ADVANCED MATERIALS
www.advmat.de

Electrochemical-Memristor-Based Artificial Neurons and Synapses—Fundamentals, Applications, and Challenges

Shaochuan Chen, Teng Zhang, Stefan Tappertzhofen, Yuchao Yang,* and Ilia Valov**

Artificial neurons and synapses are considered essential for the progress of the future brain-inspired computing, based on beyond von Neumann architectures. Here, a discussion on the common electrochemical fundamentals of biological and artificial cells is provided, focusing on their similarities with the redox-based memristive devices. The driving forces behind the functionalities and the ways to control them by an electrochemical-materials approach are presented. Factors such as the chemical symmetry of the electrodes, doping of the solid electrolyte, concentration gradients, and excess surface energy are discussed as essential to understand, predict, and design artificial neurons and synapses. A variety of two- and three-terminal memristive devices and memristive architectures are presented and their application for solving various problems is shown. The work provides an overview of the current understandings on the complex processes of neural signal generation and transmission in both biological and artificial cells and presents the state-of-the-art applications, including signal transmission between biological and artificial cells. This example is showcasing the possibility for creating bioelectronic interfaces and integrating artificial circuits in biological systems. Prospectives and challenges of the modern technology toward low-power, high-information-density circuits are highlighted.

1. Introduction

Semiconductor electronics is indubitable the most understood and well-modeled technology of our time and revolutionized our everyday lives. The most prominent example of the success of electronics is the metal–oxide–semiconductor field-effect transistor. Semiconductor devices and their high-performance in information processing have been supported by the development of super-integration based on ultrafine processing technology. Today this progress still continues in line with Moore's law.[1–3] However, in recent years, concerns and challenges have appeared about the technical limits of the associated ultrafine processing and the physical limits of transistor operations.[4–7] In addition, the von Neumann architecture of traditional digital computers encounter significant energy and time losses for shuttling data between the memory and processing units (von Neumann bottleneck).[8] Thus, current information and communication technologies (ICT) consume over 8% of the world

S. Chen
Institute of Materials in Electrical Engineering 2 (IWE2)
RWTH Aachen University
Sommerfeldstraße 24, 52074 Aachen, Germany

T. Zhang, Y. Yang
Key Laboratory of Microelectronic Devices and Circuits (MOE)
School of Integrated Circuits
Peking University
Beijing 100871, China
E-mail: yuchaoyang@pku.edu.cn

The ORCID identification number(s) for the author(s) of this article can be found under https://doi.org/10.1002/adma.202301924

DOI: 10.1002/adma.202301924

S. Tappertzhofen
Chair for Micro- and Nanoelectronics
Department of Electrical Engineering and Information Technology
TU Dortmund University
Martin-Schmeisser-Weg 4-6, D-44227 Dortmund, Germany
E-mail: stefan.tappertzhofen@tu-dortmund.de

Y. Yang
School of Electronic and Computer Engineering
Peking University
Shenzhen 518055, China

Y. Yang
Center for Brain Inspired Intelligence
Chinese Institute for Brain Research (CIBR)
Beijing 102206, China

I. Valov
Peter Grünberg Institute (PGI-7)
Forschungszentrum Jülich
Wilhelm-Johnen-Straße, 52425 Jülich, Germany
E-mail: i.valov@fz-juelich.de

I. Valov
Institute of Electrochemistry and Energy Systems "Acad. E. Budewski"
Bulgarian Academy of Sciences
Acad. G. Bonchev 10, 1113, Sofia Bulgaria

electricity, predicted to increase to over 20% by 2025.[9] To address the continuing demand for improved performance in respect on the development of Big-data computing, IoT and AI, a new qualitative paradigm shift is needed to develop devices with functions that conventional electronics cannot realize by simultaneously reducing the operation energy.[10–13] Solid-state nanoionics enhanced electronic devices are considered to be capable of providing this qualitative shift.[14–17]

Due to the size and mass of the ions, ionics was initially considered not to be competitive with conventional electronics. The vast difference in basic physical properties of ions and electrons such as size, mobility, relativistic behavior, and available charge states makes the approaches and conditions for their implementation in solid-state devices and related technologies apparently contrasting. However, remarkable advances in nanotechnology in recent years enabled to control ion transport on the nanoscale, and even the atomic-scale, and facilitated to fabricate devices that operate with localized ion transport.[15,17–21] Since these devices allow operating speeds comparable to conventional semiconductor devices, nanoionics devices have attracted attention as novel concepts for the development of information and communication devices. Functions achieved by skillfully utilizing the very nature of nanoionics demonstrated the potential to create devices that are not bound by conventional concepts.

Implementing ionic effects in nanoelectronics has the prospective to provide significant advantages and new opportunities for modern technology, such as AI or IoT. Ions were found effective to tune multiferroic properties, superconductor transition temperatures, interfacial Schottky barriers, bandgaps, and conductivity in electronic devices.[20,22–26] Chemical and physical properties of ions can be varied in a wide range by simply using different species and/or conditions, thus enabling to be adapted to different demands and applications. Ionics-based devices can operate in a wide temperature range[27–29] and are mostly resistant against undesirable effects caused by X-rays, cosmic, high energy(e.g., space technologies, health, etc.).[30] Nanostructured ionic materials and devices enable crucial advantages, such as faster reaction times due to shorter diffusion lengths and field enhanced kinetics leading to increased velocity of ion movements (even in insulators) at the nanoscale.[31] Furthermore, ions, in contrast to electrons, can be kept in small constrictions, as they cannot tunnel and easily escape. Memristors allow for various applications such as non-volatile memories, selector devices, neuromorphic computing, field programmable gate arrays, sensors etc.[32–51] They allow for information processing and storage at the same physical place (non von Neumann computer architectures) and are believed to be the key component for realizing the dreamed brain-inspired hardware paradigm shift.[11–13,52–56]

Memristors are a prominent example for the amazing fusion between nanoionics and nanoelectronics. The most important advantage of using nanoionic memristive devices is their ability to mimic the functions of biological neurons and synapses and in more wide sense biological functions. The main reason for this behavior is the common electrochemical fundamentals. Inorganic nanoionics systems can exhibit similar dynamic processes as biological systems, and the underlying kinetic and energy factors that drive the inorganic nanoionics systems have counterparts in biologic systems. For example, it has been demonstrated that starting from an unstructured state, the inorganic system can evolve into an ordered state depending on the external stimuli.[18] This process is similar to the self-assembly process in inorganic compounds, although we note that in the redox-based memrisitve systems the self-organization is driven by electrochemical processes at the individual ion level, and are strongly modulated by external stimuli—in this case electrical pulses. Migration of ions in these inorganic systems is described by similar dynamic equations that describe the molecular processes in biological systems, where different state variables in the inorganic system can be used to emulate the effects of Ca^{2+} and neuroreceptors in a biological synapse.[23,57–60] These effects were expanded to network levels in the form of crossbar structures with large connectivity.[59–68]

Thus, we can safely conclude that artificial systems can exhibit fundamental properties of life including order, response to stimuli, metabolism, homeostasis, growth, heredity, and reproduction. Underlying similarities between the artificial system and the biological system are due to the same fundamental background, such as chemical, electrical, and electrochemical potential gradients, related in dynamical equilibria and being dependent on additional thermodynamic factors such as temperature and pressure.

Current development and implementation of memristive technologies, using the unique properties of the nanoionic electrochemical systems is fast progressing worldwide. China, USA, Korea, and Japan are making huge investments in these technologies. Largest ICT companies such as Intel, Panasonic, HP, Toshiba, and Samsung are working intensively on products for the market. Recently the Japanese company NEC as the largest producer of space satellites has introduced memristive technology in their satellites, named NanoBridge-FPGA.[48,69–71]

The physical mechanisms of memristive behavior and applications of memristive devices as artificial neurons and synapses in artificial neural networks and as building units for in-memory computing have been summarized in previous work.[55,72–82] Here, the fundamental physical chemical mechanisms, device behavior, and implementation of neuronal and synaptic plasticity using memristive devices have been introduced in more detail. Specially, this review aims to present in a comprehensive matter the fundamentals and basic functions of biological and artificial neurons and synapses and discuss the driving forces beyond their operation. The common electrochemical background will be explained and discussed as the crucial point justifying their identical behavior and possibilities for control and design. Examples of the success of practical the implementation of artificial neurons and synapses and even physical connections and signals exchange between biological and artificial cells will be highlighted.

2. Working Principles of Biological Neurons and Synapses

Our modern understanding of how the human's nervous system works was first shaped by the serendipitous discovery that nerves can be stimulated by electricity in the second half of the 18th century. It took another few decades until Alan Hodgkin and Andrew Huxley made groundbreaking contributions to the understanding of how neurons, one of the key elements of our nervous system, work in detail by studying squid giant axons.[83] A neuron is

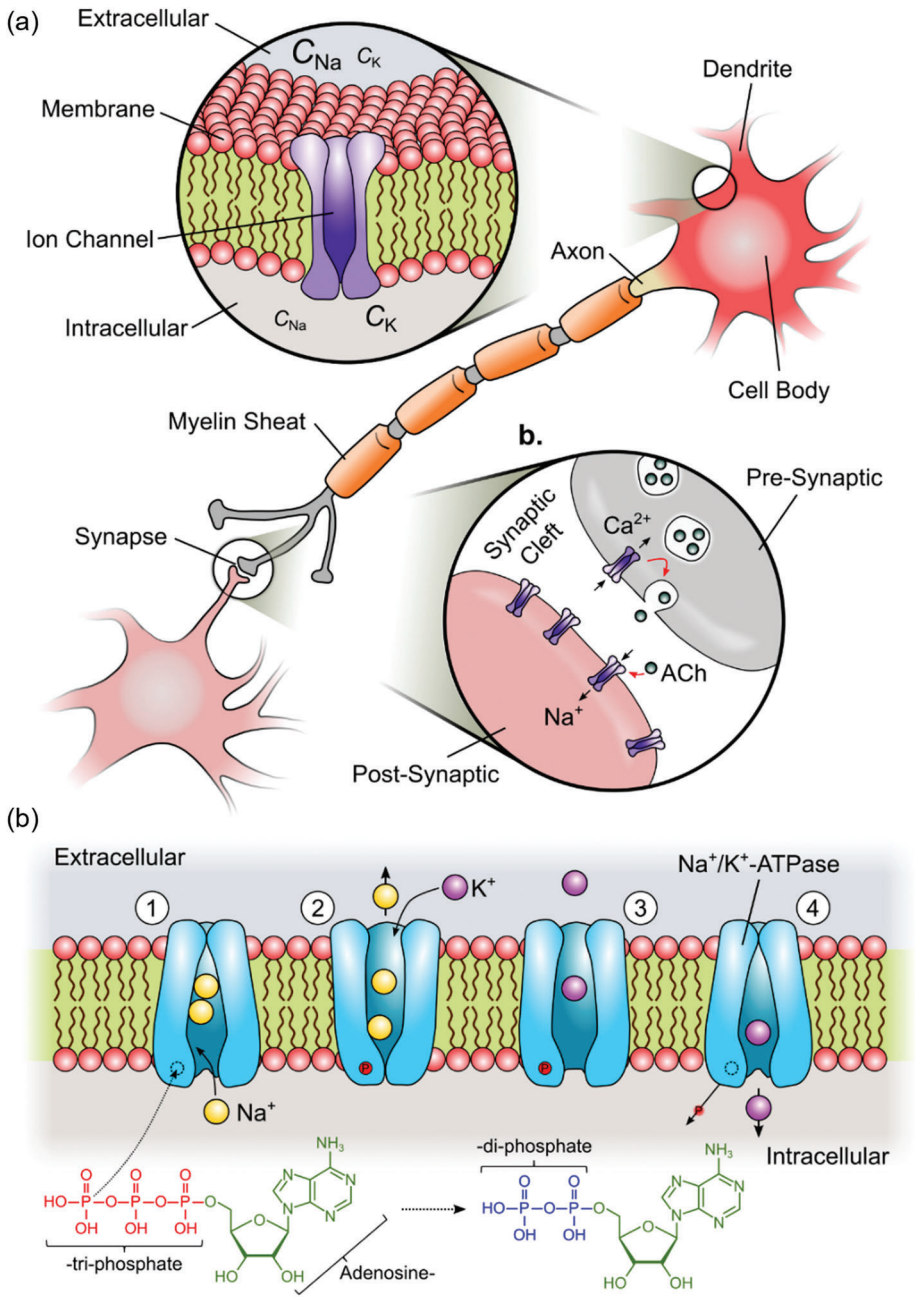

Figure 1. Basic working principle of a neuron and synapse. a) Schematic of two synaptically connected neurons. The top inset is a zoom into cross-section of the neuron's membrane. C_{Na} and C_K are the sodium and potassium-ion concentration of the extra- and intracellular medium, respectively. A voltage-controlled Na^+-ion channel is exemplarily shown. The bottom inset depicts a zoom of the synapse between both neurons. b) Zoom into the synaptic cleft between the pre- and post-synaptic side. c) Schematic of the sodium–potassium ATPase. Between steps (1) and (4) Na^+- and K^+-ions are pumped against their intra- and extracellular concentration gradients.

formed by a membrane that encapsulates the intracellular cytoplasm (**Figure 1**a).

Important components within the cytoplasm are the nucleus, ribosomes, and mitochondria among others. The nucleus is a large structure with a diameter of a few micrometers, that can be easily identified by optical microscopy. Its main role is to store the cell's genetic information and to control its metabolism via ribosome biogenesis. Ribosomes and mitochondria can be considered as microscale biochemical machines, respectively. While ribosomes perform protein synthesis, mitochondria are the cell's internal power plants. The connection between neurons is established by synapses, which typically outnumber neurons by three orders of magnitude. Between the so-called synaptic cleft, information is transmitted by electric stimuli and/or neurotransmitters (Figure 1b). In general, these processes involve a transformation of chemical into electrical energy or vice versa and are

Table 1. List important ionic species, their concentration and individual Nernst potentials at room temperature.[84,85].

Ion species	Concentration (mmol L^{-1} in H_2O) Intracellular	Extracellular	Nernst potential [mV]
Na^+	12	145	+64.4
K^+	150	4.5	-90.7
Cl^-	10	115	+63
Ca^{2+}	0.0001	1.5	+124.5
Mg^{2+}	0.5	0.5	0
HCO_3^-	10	25	+23.7
H^+	0.0001	0.00004	-24

defined as electrochemical in nature, following the fundamental laws of physical chemistry.

2.1. Electro(Chemical) Physiology of the Cell Membrane

Biological cells adopted the chemical environment in which life is believed to originate, namely salt water. The cell membrane (Figure 1a) separates the extracellular environment with a relatively high sodium and chloride ion concentration from the cytoplasm, which contains a high concentration of potassium ions. There are also other electrochemically active ions found in the cytoplasm and environment, such as Ca^{2+} and HCO_3^-. Important ionic species and their typical extra- and intracellular concentrations are given in **Table 1**. The concentration of ionic species A in the cytoplasm (intracellular) is denoted as $[A]^{I}$, whereas the extracellular concentration of the same species will be denoted as $[A]^{II}$, respectively. For example, in Table 1 we find $[Na^+]^{I} = 12$ mmol L^{-1} and $[Na^+]^{II} = 145$ mmol L^{-1} in H_2O.

The acting electrochemical force is exemplarily considered for the case of sodium ions. The electrochemical potential $\tilde{\mu}_{A,i}$ of a species A (here Na^+) on each side $i \in \{I,II\}$ of the membrane is written as:

$$\tilde{\mu}_{A,i} = \mu^0_{A,i} + RT \cdot \ln a_{A,i} + z_{A,i} F \varphi_{A,i} \quad (1)$$

where R is the universal gas constant, F is the Faraday constant, T is the absolute temperature, $a_{A,i}$ the chemical activity (directly related to concentration), z is the valence (charge) number, $\varphi_{A,i}$ is the electrical potential and $\mu^0_{A,i}$ is the standard chemical potential of species A on side i, respectively. For the particular case, the activity of sodium ions can be replaced by the ion concentration, i.e., $a_{A,i} \propto [A]^i$. This is true for all ion species listed in Table 1. In addition, at electrochemical equilibrium we define $\tilde{\mu}_{A,I} = \tilde{\mu}_{A,II}$, corresponding to:

$$\mu^0_{A,I} + RT \cdot \ln [A]^{I} + z_{A,I} F \varphi_{A,I} = \mu^0_{A,II} + RT \cdot \ln [A]^{II} + z_{A,II} F \varphi_{A,II}. \quad (2)$$

Equation (2) can be further simplified: the charge number z and standard chemical potential of the ionic species A are equal on both sides, i.e., $z_{A,I} = z_{A,II} = z_A$ and $\mu^0_{A,I} = \mu^0_{A,II}$. Rearrangement of Equation (2) leads to:

$$z_A F \cdot (\varphi_{A,I} - \varphi_{A,II}) = RT \cdot \ln \left(\frac{[A]^{II}}{[A]^{I}} \right) \quad (3)$$

Equation (3) demonstrates that the chemical and electrical force are in balance, where each change in the concentration of one component results in a change in the electrical potential difference and vice versa. The electrical potential difference between the extracellular and intracellular $\varphi_{A,I} - \varphi_{A,II}$ is referred to as the equilibrium potential $\Delta\varphi_A$ for a specific ionic species A. By replacing $\varphi_{A,I} - \varphi_{A,II}$ with $\Delta\varphi_A$ we obtain:

$$\Delta\varphi_A = \frac{RT}{z_A F} \cdot \ln \left(\frac{[A]^{II}}{[A]^{I}} \right) \quad (4)$$

Equation (4) is also known as the Nernst equation.[86] For example, in case of sodium ions (A = Na^+), with $[Na^+]^{I} = 12$ mmol L^{-1}, $[Na^+]^{II} = 145$ mmol L^{-1}, $RT/F \approx 25.8$ mV at room temperature, and $z_{Na^+} = 1$ we find $\Delta\varphi_{Na^+} = 64.4$ mV.

2.1.1. Resting Potential

At this point, we only considered the equilibrium condition for a single ionic species (here Na^+) assuming no ionic transmembrane net flux. In the real cells, Nernst potentials for all species showing the concentration gradients across the membrane are formed (Table 1), resulting in a superposition of these individual Nernst potentials, that finally differs from the single ion case example. This also changes the magnitude of the driving force, leading to a transmembrane penetration of ions, aiming to reach a new equilibrium condition accounting for all relevant ions. This process is a diffusion process in nature, and the corresponding ion diffusion flux $j_{A,Diff}$ is described by Fick's first law:

$$j_{A,Diff} = -D_A \cdot \frac{d[A]}{dz} \quad (5)$$

Here, D_A is the diffusion coefficient for ionic species A and $d[A]/dz$ is the transmembrane ion concentration gradient. For simplicity, we assume a 1D ion diffusion process. At the same time, the electric field across the membrane will induce an ion drift flux $j_{A,Drift}$:

$$j_{A,Drift} = e z_A n_A \mu_A E_M \quad (6)$$

where e is the elementary charge, n_A the number and μ_A the mobility of charge carrier A, and E_M the electrical field across the membrane. z_A is the valence of the charge carriers. With the Einstein relation we can express the mobility by the ionic diffusion coefficient, the Boltzmann constant k, the temperature, and the elementary charge:

$$\mu_A = D_A \frac{e}{kT} = D_A \frac{F}{RT} \quad (7)$$

We may simply replace the number of charge carriers by the ion concentration, i.e., $n_A = [A]$. Moreover, the transmembrane electric field is given by the voltage drop across the membrane $\Delta\varphi_M$ and the membrane's thickness L: $E_M = \Delta\varphi_M / L$. The total net flux j_A for the ionic species A is given by a superposition of the diffusion and drift fluxes:

$$j_A = j_{A,Diff} + j_{A,Drift} = D_A \cdot \left(\frac{z_A F}{RT} \frac{\Delta\varphi_M}{L} [A] - \frac{d[A]}{dz} \right) \quad (8)$$

Equation (8) is a differential equation of first order of the form:

$$\frac{\mathrm{d}[A]}{\mathrm{d}z} = a[\mathrm{A}] + b \tag{9}$$

The boundary conditions for this differential equation are [A] = $[A]^{\mathrm{I}}$ (i.e., concentration in the cytoplasm) for $z = 0$, and [A] = $[A]^{\mathrm{II}}$ for $z = L$ (i.e., extracellular ion concentration). By integration across the membrane from $z = 0$ to $z = L$ we obtain:

$$j_{\mathrm{A}} = z_{\mathrm{A}}^2 \frac{F\Delta\varphi_{\mathrm{M}}}{RT} \cdot \frac{D_{\mathrm{A}}}{L} \cdot \frac{[A]^{\mathrm{II}} - [A]^{\mathrm{I}} \cdot \exp\left(-\frac{z_{\mathrm{A}}F\Delta\varphi_{\mathrm{M}}}{RT}\right)}{1 - \exp\left(-\frac{z_{\mathrm{A}}F\Delta\varphi_{\mathrm{M}}}{RT}\right)} \tag{10}$$

We define $P_{\mathrm{A}} = D_{\mathrm{A}}/L$ to be the membrane's permeability for a given ion A. In a steady state, the ideal total flux across the membrane is zero:

$$j = 0 = \sum_{\mathrm{A}} j_{\mathrm{A}} \tag{11}$$

This condition is satisfied for only a single voltage value $\Delta\varphi_{\mathrm{M}}$, the resting membrane potential:[87]

$$\Delta\varphi_{\mathrm{M}} = \frac{RT}{F} \cdot \ln\left(\frac{\sum_{\mathrm{Cations}} P_{\mathrm{A}}[\mathrm{A}]^{\mathrm{II}} + \sum_{\mathrm{Anions}} P_{\mathrm{A}}[\mathrm{A}]^{\mathrm{I}}}{\sum_{\mathrm{Cations}} P_{\mathrm{A}}[\mathrm{A}]^{\mathrm{I}} + \sum_{\mathrm{Anions}} P_{\mathrm{A}}[\mathrm{A}]^{\mathrm{II}}}\right) \tag{12}$$

Instead of absolute permeabilities P_{A}, it is useful to express Equation (12) with relative permeabilities $p_{\mathrm{A}} \propto P_{\mathrm{A}}$. For simplicity, we now assume that only the cations Na^+, K^+, and the anion Cl^- are dominating:[87]

$$\Delta\varphi_{\mathrm{M}} = \frac{RT}{F} \cdot \ln\left(\frac{p_{\mathrm{Na^+}}[\mathrm{Na^+}]^{\mathrm{II}} + p_{\mathrm{K^+}}[\mathrm{K^+}]^{\mathrm{II}} + p_{\mathrm{Cl^-}}[\mathrm{Cl^-}]^{\mathrm{I}}}{p_{\mathrm{Na^+}}[\mathrm{Na^+}]^{\mathrm{I}} + p_{\mathrm{K^+}}[\mathrm{K^+}]^{\mathrm{I}} + p_{\mathrm{Cl^-}}[\mathrm{Cl^-}]^{\mathrm{II}}}\right) \tag{13}$$

Equation (13) is the so-called Goldman–Hodgkin–Katz equation. It has been experimentally verified that K^+ and Cl^- are carrying most of the ionic current in neurons. We set $p_{\mathrm{K^+}} = 1$, $p_{\mathrm{Cl^-}} = 0.1$, and $p_{\mathrm{Na^+}} = 0.03$.[87,88] With the concentrations given in Table 1 and a body temperature of 37 °C (= 310 K) we find a resting potential of $\Delta\varphi_{\mathrm{M}} = -75$ mV versus extracellular medium. This value is in good agreement to what can be experimentally measured.[86] The resting potential is therefore close to the K^+ equilibrium potential.

2.1.2. Saving the Concentration/Potential Gradient (Sodium–Potassium ATPase)

Ideally, the total transmembrane ionic flux is zero. But in reality, a small ionic leakage of sodium and potassium ions crossing the membrane is existing, directed to neutralize the concentrations gradients over time, which would lead to a degeneration of the neuron. Keeping the ion concentration gradients constant (and thus, the intrinsic electric potential), an additional active process is involved, known as the sodium-potassium ATPase. The process is also denoted as Na/K-pump and a schematic presentation of the operation principles is shown in Figure 1c.

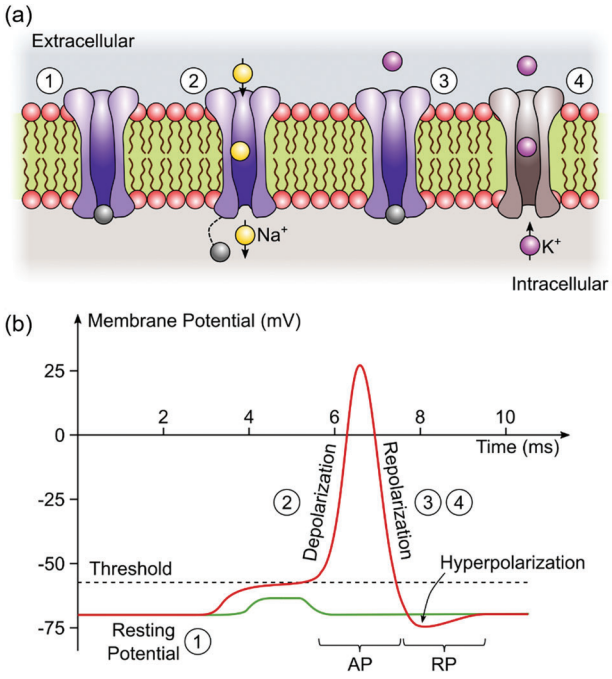

Figure 2. Generation of action potentials. a) Illustration of a voltage-controlled Na^+-ion channel at rest potential (1), during depolarization (2) and repolarization (3), respectively. A K^+-ion channel is depicted in (4). b) Transient characteristic of an action potential (red) and a stimulation that does not trigger an action potential (green).

2.2. Generation and Transmission of Electro(Chemical)Physiologic Signals

The cell's membrane is suppressing most of the ionic current, making the absolute permeabilities quite low, leaving only a small ionic leakage current persistent. On the local scale, parts of the membrane can act as a gate for transmembrane ion exchange. These parts are termed as ion channels, which are ion-selective proteins and can control the ion movement. There are different types of ion channels. The most important ion channels are voltage-controlled channels and Ca^{2+}-triggered channels. Voltage-controlled channels open upon applying a certain membrane potential above a threshold-level. In case of Ca^{2+}-triggered channels, presence of Ca^{2+}-ions triggers opening of the ion channels. There are also leakage channels, that allow transmembrane ion exchange at rest. The membrane permeability for an ion is related to the number of open ion channels. Though the absolute number of open ion channels is small at rest, the relative number of open K^+ leakage channels is much larger than of any Na^+ channels, which results in relative permittivity of $p_{\mathrm{K^+}} = 1$ compared to $p_{\mathrm{Na^+}} = 0.03$.[87,88]

2.2.1. Action Potentials

At rest, the voltage-controlled ion channels are closed, **Figure 2**a-1. We now consider that the membrane potential of a neuron is suddenly increased above a certain threshold level, typically at about -55 mV. This opens fast voltage-controlled Na^+ channels, Figure 2a-2. Eventually, Na^+ ions move into the

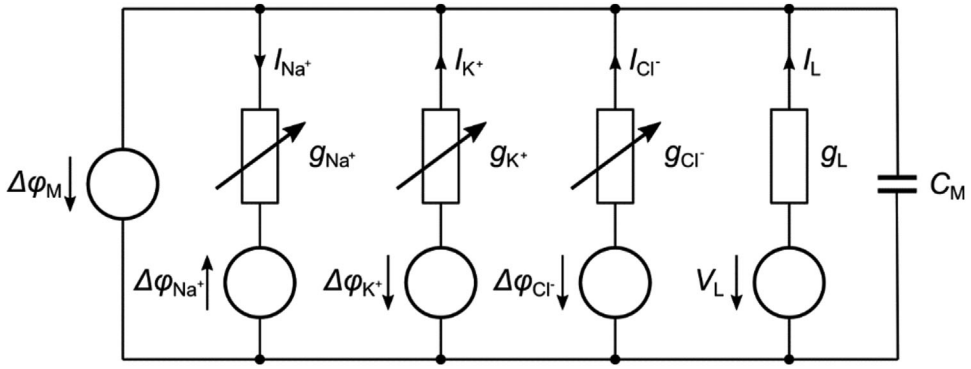

Figure 3. Equivalent circuit of the Hodgkin–Huxley model. VM and CM are the membrane potential and capacity. $\Delta\varphi_{Na^+}$, $\Delta\varphi_{K^+}$ and $\Delta\varphi_{Cl^-}$, and g_{Na^+}, $g_{Na^+}$and g_{Cl^-}, are the Na^+, K^+ and Cl^- overpotentials and ionic conductance, respectively. V_L and g_L are the leak potential and conductance.

cell due to the concentration gradient. This will increase the membrane potential towards the Nernst potential of Na^+ and results in the generation of an action potential (AP, Figure 2b). A positive feedback loop will open more and more Na^+ channels. Since $\Delta\varphi_M$ logarithmically depends on p_{Na^+}, p_{Na^+} must change by orders of magnitude and for a short time $p_{Na^+} > p_{K^+}$. This process is called depolarization. After a short time (usually some 1–2 ms), the Na^+ channels become inactive and get closed. This will stop further Na^+ transport into the cell. Now, slow voltage-controlled K^+ channels open and allow for transport of K^+ out of the cell. Evidentially, the membrane potential will decrease. We call this process repolarization. Since the permeability for K^+ is now larger than during rest, the membrane potential will be subject to a short undershoot effect (hyperpolarization) until the voltage-controlled K^+ channels become inactive. The Na^+ channels remain inactive for a while (refractory period, denoted as RP in Figure 2b), during which the cell cannot trigger a new action potential. Over time, the sodium-potassium ATPase will restore the initial ion concentration gradients. The positive feedback loop ensures that once the cell is stimulated above the threshold level, the depolarization continues irrespective of any external influence. If the potential is below the threshold voltage the Na^+ permeability is not sufficiently increased, and the cell returns to the resting potential without triggering an action potential. It is noteworthy that the shape and amplitude of an action potential do not depend on the stimulation signal, once the threshold potential has been exceeded. Thus, the depolarization process can be considered as an "all or nothing" event.

2.2.2. The Hodgkin–Huxley Model

The initiation and propagation of action potentials in neurons can be modeled using the Hodgkin–Huxley model.[83,89] It is based on a parallel circuit composed of the cell membrane's capacity $C_M = C'_M \cdot l$ (where l is the length of the membrane and $C'_M \approx 1\ \mu F\ m^{-1}$),[90] and a number of non-linear conductance, which are connected in series to voltage sources as shown in **Figure 3**. Each series connection of a conductance and voltage source represents voltage-controlled ion channels (i.e., g_{Na^+} and g_{Na^+} for the Na^+- and K^+-ion channels) and the respective electrochemical gradient (Table 1).[91] $g_L = 0.3$ mS cm^{-3} and $V_L = -54.4$ mV[91] were originally introduced to model other ions.[83] Nowadays, g_L and V_L are denoted as leakage conductance and leakage potential. I_P represents the sodium-potassium ATPase and $\Delta\varphi_M$ is the membrane potential.

Using the voltage-clamp method,[92] Hodgkin and Huxley derived expressions for sodium and potassium conductance:

$$g_{K^+} = \bar{g}_{K^+} \cdot n^4 \text{ and } g_{Na^+} = \bar{g}_{Na^+} \cdot m^3 \cdot h \tag{14}$$

where $\bar{g}_{K^+} = 36$ mS cm^{-3} and $\bar{g}_{Na^+} = 120$ mS cm^{-3} are the maximum conductances measured during an action potential, and n, m, $h = 0...1$ are gating variables, which describe activation and inactivation of ion channels.[91] g_{Na^+} requires two different gating variables m and h to describe the fast activation and delayed inactivation. The membrane potential obeys the following differential equation:

$$C_M \cdot \frac{d\Delta\varphi_M}{dt} = I_P - I_{K^+} - I_{Na^+} - I_L \tag{15}$$

For the K^+- and Na^+-ion current we find

$$I_{K^+} = g_{K^+} \cdot \left(\Delta\varphi_M - \Delta\varphi_{K^+}\right) \text{ and } I_{Na^+} = g_{Na^+} \cdot \left(\Delta\varphi_M - \Delta\varphi_{Na^+}\right) \tag{16}$$

Based on the experimental findings, we may express the gating variables as follows:

$$\frac{dn}{dt} = \alpha_n\left(\Delta\varphi_M\right) \cdot (1-n) - \beta_n\left(\Delta\varphi_M\right) \cdot n \tag{17}$$

$$\frac{dm}{dt} = \alpha_m\left(\Delta\varphi_M\right) \cdot (1-m) - \beta_m\left(\Delta\varphi_M\right) \cdot m \tag{18}$$

$$\frac{dh}{dt} = \alpha_h\left(\Delta\varphi_M\right) \cdot (1-h) - \beta_h\left(\Delta\varphi_M\right) \cdot h \tag{19}$$

α_n, α_m and α_h are exponential functions. By using Equations (15) and (16–19) we find a non-linear differential equation, which cannot be analytically solved. But by choosing appropriate values for all constants, the numerical simulations show similar transient currents compared to measured action potential.

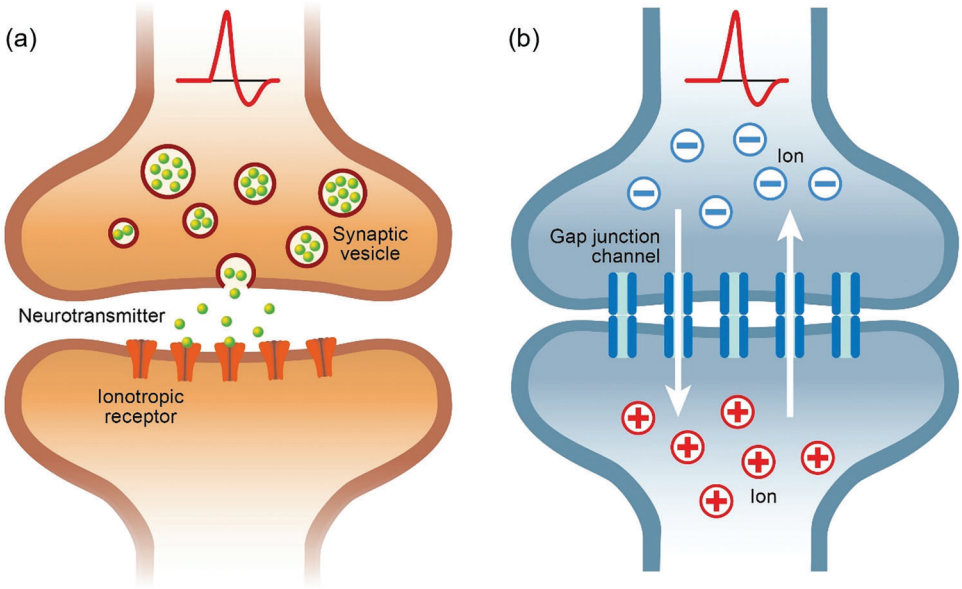

Figure 4. a,b) Basic structure and operation of chemical synapses (a) and electrical synapses (b).

2.2.3. Signal Transmission and Synapses

Neuronal information is processed by the transmission of the action potential. After initiation of the electric signal due to different types of stimuli, neurons transmit signal further to other neurons. This information processing between two or more neurons is performed by synapses. A synapse connects a pre-synaptic to a post-synaptic neuron (see **Figure 4**). Generally, two different types of synapses can be distinguished—chemical and electrical.

In case of chemical synapses (Figure 4a), information transmission involves signal propagation from a neuron to and across a chemical synapse, by changing the electric impulse to chemical response that in turn is transformed back into an electric signal.[93] The signal (i.e., the action potential) is directed along the neuron's axon (nerve fiber) toward synapses. A synapse connects the axon of a pre-synaptic neuron (also known as axon terminal) and a dendrite of a post-synaptic neuron. The cell body (soma) of the presynaptic neuron and its axon are connected by the axon hillock. The role of the axon hillock is to sum up action potentials before propagating across the axon. This signal propagation is enabled by local generation of action potentials across the axon. The action potential is generated at $x = x_0$. and will potentially increase the local membrane potential nearby x_0. If the membrane potential at $x = x_1$ is above the threshold potential, a new action potential will be generated at x_1. Due to the refractory phase of Na^+ channels, signal propagation takes place in only one direction. However, this signal propagation is relatively slow and works only for short distances. Faster signal propagation towards a synapse is provided by myelin sheaths,[94] which act as insulators and only allow for generation of an action potential between two neighboring myelin sheaths. Signal propagation is now provided by the electric field that jumps across the myelin sheaths.

Once the signal reaches the pre-synaptic axon terminal (presynaptic spike), neurotransmitters (acetylcholine, ACh) are released into the synaptic cleft. In the presence of neurotransmitters, receptors on the post-synaptic dendrite open Na^+-ion channels. The influx of Na^+ will then generate an action potential on the post-synaptic neuron (post-synaptic spike). Initially, the neurotransmitters are kept in synaptic vesicles on the pre-synaptic side. Once the pre-synaptic side is stimulated voltage-controlled Ca^{2+}-ion channels are opened. The influx of Ca^{2+} triggers the vesicles to release the neurotransmitters into the synaptic cleft. After signal propagation across the synapse, these vesicles are again regenerated.

The strength of the synapse (connection between two neurons) can be modeled by a weighting factor Δw. Δw is large if there is a strong link between the neurons, that is, an action potential of the pre-synaptic neurons propagates across the synapse and stimulates the post-synaptic neuron. Δw can be also small so if there is no or only a weak junction between both neurons. The ability of neurons to adjust the strength of the connection (synapses) between two and more neurons is defined as neuroplasticity.[95] The biological process that is responsible for this ability is known as spike-timing-dependent plasticity[57,96,97] (STDP) and is schematically depicted in **Figure 5**. STDP describes that the change Δw of the weighting factor between two neurons (A) and (B) is a function of the time difference between the pre- and postsynaptic stimulation. When the pre-synaptic neuron (A) is stimulated at first and the post-synaptic neuron (B) is stimulated shortly afterwards, Δw is increased (long term potentiation, LTP). However, the post-synaptic neuron (B) may be also connected to other neurons (X) that allow for stimulation, which is not correlated to a stimulation of neuron (A). In this case, Δw is decreased (long term depression, LDP). LTP and LDP are important processes that allow neuronal signal processing and learning. Biologically, LTP and LDP are due to an increase/decrease of the neurotransmitters, Ca^{2+}-ion channels and ACh-receptors.

Electrical synapses have much simplified structure (Figure 4b), practically no delay (very fast) signal transmission

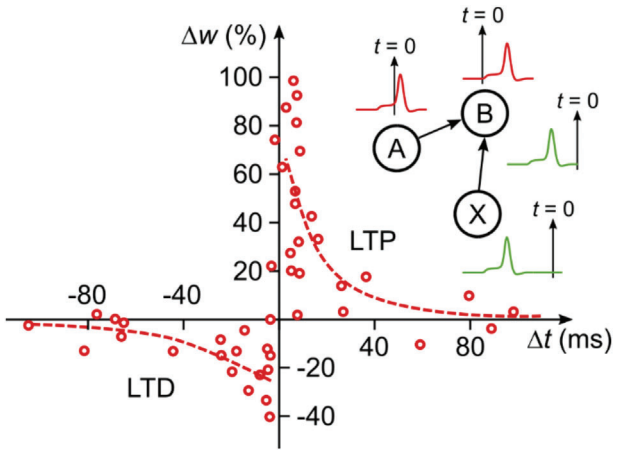

Figure 5. Illustration of spike-timing-dependent plasticity by a change of the weighting factor as a function of the time difference Δt between pre- (A) and post-synaptic (B) spikes. An additional neuron (X) is shown, which can stimulate neuron (B) without any correlation to a stimulation by neuron (A). Reproduced with permission.[98] Copyright 1998, Society for Neuroscience.

and synchronous action and are bidirectional, allowing for a direct charge (ion) transport. They are less common but are present in all animals' nervous systems, found typically in the cardiovascular system, retina, and hormone secreting neurons. They are spread in neuromuscular junctions where rapid responses are essential. In electrical synapses, the pre- and post-synaptic side are connected by pores on the cell membrane, which are called gap junctions (also known as intracellular gap). These dynamic gap-junctions have a diameter of 1.6–2 nm and are much shorter (2–4 nm) compared to the synaptic cleft of chemical synapses (typically 20–40 nm).[99,100] These are intercellular connections of the cytoplasm of two cells, that allow electrical signals to be transmitted across two neurons. In contrast to chemical synapses, gap junctions allow direct charge transport, i.e., for transport of ions, and molecules such as metabolites or intracellular messengers with a molecular weight of up to 1 kDa.[101] Here, the mass transport is a diffusion-controlled process, which is typically bidirectional in contrast to chemical synapsis, where signal transmission is unidirectional. Electrical synapses can also be effectively rectifying by opening/closing upon a change of the membrane potential or electrochemical ambient (such as high extracellular Ca^{2+}-concentration or low pH-value).[101] Synaptic plasticity has been intensively studied for chemical synapses,[102] but similar behavior is also reported for electrical synapses,[103] which are much faster but not as complex as chemical synapses.

3. Artificial Neurons and Synapses

Using advantages and functions of biological nervous system for data processing can proceed in two fundamentally different approaches.

The first way is reproducing the function(s) only, without considering reproducing the mechanism. For example—the action potential in a neuron can be generated directly by applying external voltage from a source. Synapses must not necessarily be a junction between two artificial neurons, and their weight must not necessarily be representing the strength of the connection (ohmic resistance) but can use other physical effects, e.g., magnetic junctions etc. This can be achieved for example by software and/or combined software/hardware approach and is currently used in classical metal–oxide–semiconductor (CMOS) architectures.

The second possibility demands reproducing the operation mechanism as well. In this case, the used cells/devices have not only the same output functionalities, but as well can physically reproduce the processes (or at least a part of them) of their biological counterparts.[55,76,104] The easiest way of creating artificial neurons and synapses and expecting the same behavior and functions is using systems/devices that operate on the same fundamental principles. In the previous section, it has been demonstrated and discussed that biological neuron cells and the connections between them (synapses) operate on electrochemical principles. Therefore, the focus should be set on electrochemical systems. These systems have the advantage that a variety of ions and electrolytes/membranes can be used for reproducing biological functions and not only Na^+, K^+, Ca^{2+} and Cl^- (as in biological cells). This makes it possible not only to mimic the functions, but also to control and/or modify them, depending on the targeted applications. One can select for example membranes/electrolytes made of various inorganic or organic/bio/polymer materials, ensuring stability and robustness in various environments and conditions. By variation of the thickness, the diffusion/response time can be tuned. Using different mobile ions (e.g., with different size, charge, mobility, etc.) and ion sources (elements, compounds, solutions, etc.) also the transport processes can be controlled. The intrinsic cell voltage can be adjusted not only by using different ion concentrations, but as well by using different electrodes, placed on both sides of the cells. In addition, the modern technology allows downscaling the cells, reaching the size and device density close to the number of neurons and synapses in the human brain. Creating artificial neurons and synapses can be understood as a replacement of one electrochemical system by another.

3.1. Electrochemical Artificial Neurons

Redox-based memristive devices (ReRAMs) devices are nanoscale electrochemical systems belonging to more the general class of resistive random access memories (RRAM), found capable in reproducing both fundamental processes and functionalities of neurons and synapses. These devices obey the same fundamental equations (e.g., (1)–(13) provided for the biological systems. The principal schematic structure of biological and artificial neurons is compared in **Figure 6**. The membrane in bio-cells (Figure 6a) is replaced by thin solid electrolyte (switching) film in Figure 6b. In a similar manner, the different ion concentrations in extra- and intracellular liquids are replaced by electrodes with different chemical potentials.

One characteristic signature of the neurons is the built-in (resting) potential, which can be adjusted for artificial cells within much larger margins (ranging from microvolts up to few volts are possible). Several terms are used by different communities describing the resting potential of one cell/device—electromotive force (emf), built-in potential or nanobattery effect. In contrast to

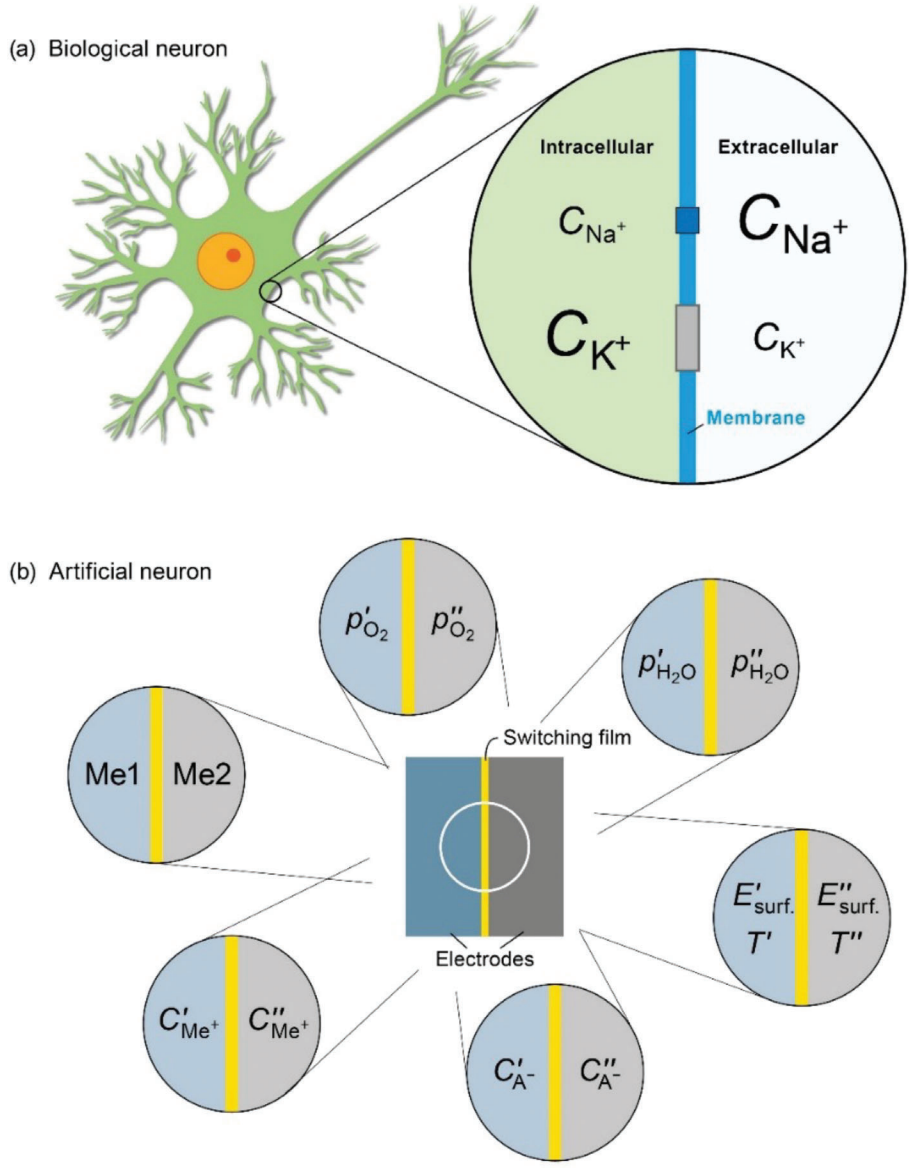

Figure 6. a,b) Origins of built-in potential (nanobattery effect) in biological (a) and artificial (b) synapses. In the case of biological neurons, the intrinsic potential is in the range of −70 mV to about −90 mV for most species. The mobility of the ions is regulated by the channels in the membrane. In artificial neurons, the emf may largely vary depending on the particular system and thermodynamic conditions. The membrane in the biological neurons is considered identical with the switching film in the memristive devices. The switching film has no channels, but different ions have different mobility in the matrix due to their different bonding, charge and size.

biological cells where the resting potential is determined mainly by Na^+/K^+ equilibria, there are several possible origins for this potential[105] in memristive cells and some examples are shown in Figure 6b. In general, any chemical asymmetry in the devices requires electrical compensation (see Equations (2) and (3)).

One of the most typical origins for the nanobattery effect is the chemical difference of the electrodes (different metals). For example, the top electrode is of Ag and the bottom of Pt. As Pt is assumed inert only Ag can be dissolved in the solid electrolyte film. The driving force will act in direction to dissolve Ag from the top electrode and deposit it at the Pt electrode. The final state would be complete covering of Pt with Ag and the time for reaching this final state will depend on the kinetics (reaction rate, mobility of Ag-ions etc.). In this situation, the neuron/memristive cell will act as a battery with the anode being the Ag electrode (negative) and Pt will be positive pole. Similar effect can be achieved by using alloys with different concentrations (activities) of the alloying element—for example AgCu alloy with different Cu content,[106] or $Cu_{2-x}S$ of different stoichiometry (Cu content),[107] etc.

Other sources for the existence of the electromotive force (built-in/resting potential) are differences in the partial pressure of oxygen or moisture at the two interfaces. This is again chemical difference of the electrodes, but the origin of this difference is not the same as with different metal electrodes. This situation

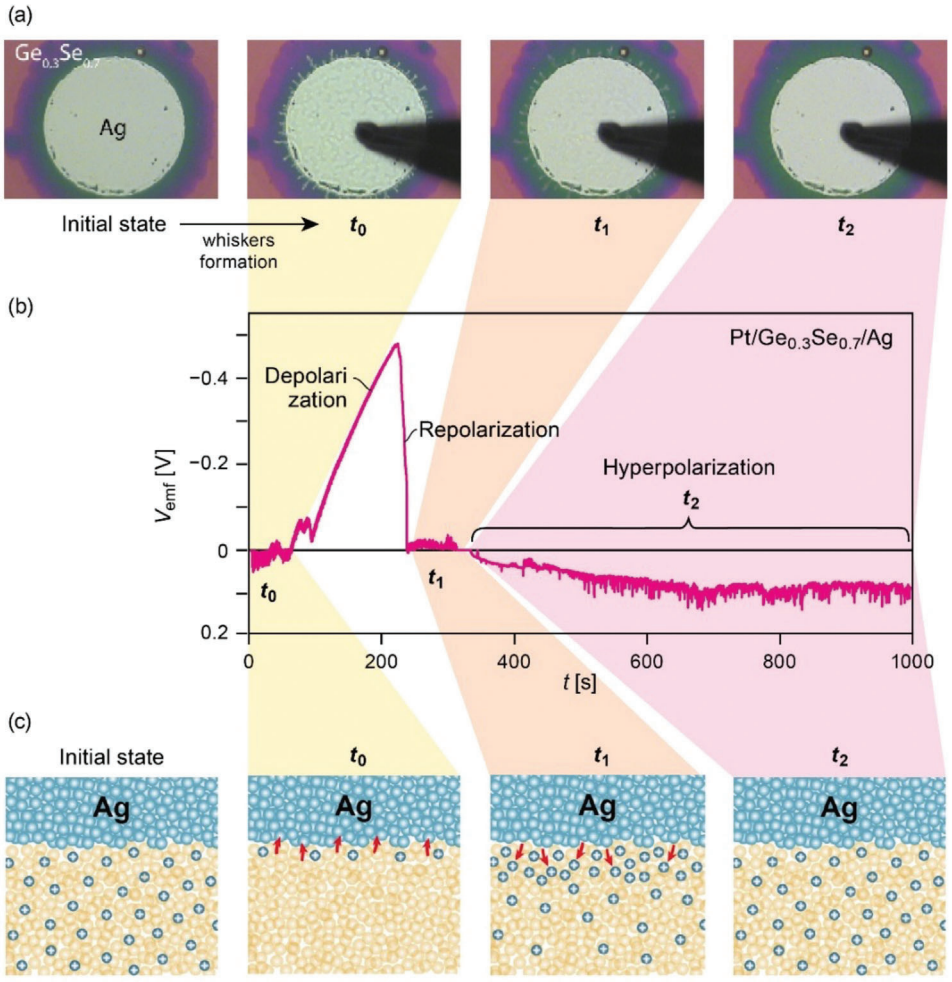

Figure 7. Operation and signal generation on an electrochemical artificial neuron based on $Ag/Ge_{0.3}Se_{0.7}/Pt$ memristive device. a) Optical images of the artificial neuron upon formation and dissolution for Ag whiskers. b) The corresponding voltage–time characteristics, recorded during the chemical processes. c) Schematic presentation of the dynamics of the concentration gradients, corresponding to the optical images and related voltage–time characteristics. a–c) Reproduced with permission.[105] Copyright 2013, Springer Nature.

can easily occur because top and bottom electrodes have different access to local environment. Thus, the oxygen partial pressure at the top electrode will be higher, as access of the gas to the electrode/electrolyte interface is easier, compared to the bottom electrode (access is much more difficult).

Differences in the surface excess energy and temperature can also result in an intrinsic potential difference. Especially important are concentration gradients of one or more charged species (cations and/or anions) within the switching film, leading to an electromotive force. In more general cases this potential is a nonequilibrium potential, as with time the concentration of the mobile species will tend to relax, thus the gradient will disappear. Such type of potential can be repeatedly created or resolved by the operation scheme of the device, as it is known that the amount of incorporated and extracted ions during the switching process is usually not equal.

It is important to note that driving forces and gradients can overlap and potentiate or diminish their effect on the total emf. This is exactly comparable to the situation of overlapping potential contributions in the biological neurons. It is worth explaining that in artificial devices this potential cannot always be measured directly by simple electrical/voltage measurements due to, for example, too high electronic conductivity or too insulating samples. Nevertheless, despite this force cannot always be directly measured, its action and effects on the system are persistent, modulating the electrical behavior and response.

An example, experimentally evidencing that system operating on same fundamental principle behaves similarly in terms of voltage/current responses is shown in Figure 6. The formation of action potential and general voltage signal in $Ag/Ge_{0.3}Se_{0.7}/Pt$ artificial neuron[105] is a function of two parallel processes of formation of potential difference that overlap. The potential-time dependence (shown in **Figure 7**) is also correlated with the optical changes in the system (captured by optical microscopy) and as well schematic presentation of the chemical changes, responsible for the electrical response.

As it can be seen, the shape of the potential–time curve (Figure 7b) is very similar (practically identical) to action

potential—time dependence of a biological neuron (Figure 2b). Specifically, the membrane potential in biological neurons can be emulated by the built-in potentials in memristive device. Thus, the functionalities of memristive devices based on artificial neurons can mimic the generation and transmission of electrophysiologic signals in biological neuronal systems, enabling the development of neuro-inspired computing systems for future AI applications.

The mechanism and the origin of such neuronal dynamic behavior in redox-based artificial neurons can be described as interplay between the Nernst and diffusion potentials.[105] For example, the artificial neuron, as prepared, has the structure $Ag/Ge_{0.3}Se_{0.7}/Pt$. $Ge_{0.3}Se_{0.7}$ dissolves chemically Ag (from the top electrode), leading to the incorporation of Ag^+ ions within $Ge_{0.3}Se_{0.7}$. This incorporation is also optically visible as a violet shade around the Ag metal electrode (Figure 7a). Thus, the initial state of the solid film is an Ag-doped $Ge_{0.3}Se_{0.7}$ where the concentration of Ag^+ is homogenously distributed within the selenide, as shown in Figure 7c. Applying a negative voltage to the Ag top electrode is casing a formation of Ag whiskers. To form the whiskers, Ag^+ ions are extracted/reduced from the film, leading to significant depletion of Ag^+ in $Ge_{0.3}Se_{0.7}$ (see stage t_0). After the current approaches zero (meaning most of the ions are extracted), we switched the voltage off and start measuring the electromotive force as shown in Figure 7b. At this point, Nernst voltage (chemically asymmetric electrodes) dominates shifting the emf to negative direction (Ag is anode). With time and due to this force Ag whiskers start to dissolve again (stage t_1 in Figure 7a), creating a concentration gradient as shown in Figure 7c. The sign of the voltage formed due to the concentration gradient is opposite to the initial one, leading to shift in the recorded potential towards positive values. The concentration of Ag^+ ions start to equilibrate going into stage t_3. The time scale is longer compared to the time scale shown for biological neurons shown in Figure 2b. The reason is the different absolute mobilities of the ions. The lower is the ion mobility the slower is the equilibration and respectively the signal relaxation. The opposite is also true—as higher the mobility as faster the equilibration/relaxation.

Of course, biological neurons show differences in absolute concentration of ions and reaction time. However, their properties cannot be varied or modulated in a large time/voltage window. In contrast, the behavior and characteristics of artificial neurons are capable of being modulated. As discussed on the example of Figure 7, one can vary several parameters, leading to change in the electrical characteristics and giving a huge advance and perspective for designing neurons according to intended applications. For example, the Nernst voltage can be varied by combining different top and/or bottom electrodes. The electromotive force formation is exactly the same as in the conventional batteries (of course accounting for the specifics of the nanosystems) and therefore, using the table for standard electrode potentials one can create neurons with differently strong initial Nernst potential.

Further degree of freedom is provided by the selection of the switching film. Its conductivity can vary not only as a function of ion-specific bonding, but also depending on electronic conductivity and several other factors such as structure, density, and thickness. For example, increasing the thickness of the solid electrolyte will slow down the equilibration of the concentration gradient and in this way the relaxation time.

Thus, artificial neurons allow for much higher flexibility in respect materials design and allow tuning of the properties in a very broad ranges of voltages and time windows. For electrodes, a variety of metals or compounds (for example TiN, ITO, FTO, etc.) can be used showing a spectrum of properties that can be varied such as stability, affinity to oxygen and standard electrode potentials. In a similar manner, for solid electrolytes inorganic, polymer, and bioinspired materials can be used having a broad range of mechanical, chemical, and transport properties. The combination of these factors provides the opportunity of designing artificial neurons on demand by proper selection and combination of the individual components of the memristive device.

The implementation of biological neuron models using solid-state electronic devices has been demonstrated not only by redox-based memristors,[105,108–112] but also using a variety of memristive systems, including phase change memories,[113–116] magnetic random access memories,[117–119] Mott memristors,[120–124] and diffusive memristors.

It should be noted that not all memristive cells show the same ionic dynamics and electrochemical processes as redox-based devices (and biological cells). In phase change devices, the processes are restricted to (re)crystallization, i.e., purely structural change. Spintronic neurons are based on purely electronic/magnetic effects, and Mott-type neurons are related to a change in the structural parameters and/or thermal runaway effects (despite involving to a certain extent ionic movements). These different types memristive devices should be considered rather to the first type devices (providing only same functionalities, but not same operation principle) or as a hybrid solution. It cannot be generalized whether their performance is better or worse compared to the redox-based devices. By such a comparison it is important to consider the offered (multi)functionalities, particular application that is targeted and as well the energy consumption and required physical space.

It should be noted that artificial neurons based on diffusive memristors have similar physical and electrochemical dynamics with redox-based artificial neurons. In diffusive memristors, integrate-and-fire dynamic is emulated by the field accelerated drift and diffusion of metal atoms, generating conductive nanofilament bridging the nanoclusters. The nanoclusters (Ag) are doped in the dielectric switching layer (i.e., HfO_x, SiO_x) prior to device programming.[58] Upon the removal of the electrical bias, the metallic nanofilament gradually dissolves in the solid electrolyte. The filament dissolution is induced by the backward diffusion of metal atoms because of interfacial energy minimization. As a result, the memristor relaxes back to virgin high-resistive state. In contrast to redox-based memristors where cation migration and nucleation processes take place during action potential integration and firing, diffusive memristors can mimic biological neuronal dynamics more efficiently as the diffusive dynamics is closer to the ionic drift and diffusion in biological neuronal systems.[125,126] Diffusive dynamics involving cation and field-induced nucleation was also found in $Cu_{0.1}Te_{0.9}/HfO_2/Pt$ type memristors.[127] Wang et al. have shown stochastic leaky integrate-and-fire artificial neuron using Pt/SiO_xN_y:Ag/Pt diffusive memristors integrated with a series capacitor.[128] Moreover, by integrating the diffusive artificial

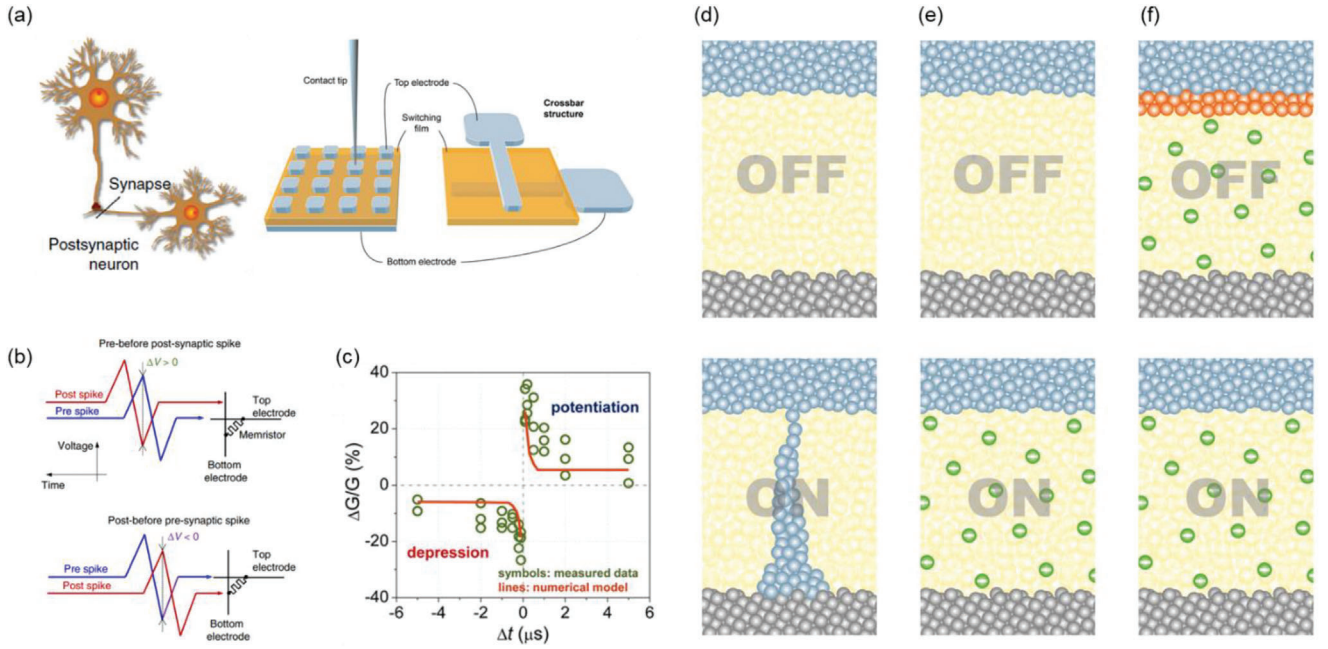

Figure 8. Artificial synapse and different mechanisms for changing the resistance (synaptic weight). a) Schematic illustration of biological synapse (left) and its implementation using a two-terminal memristive device (right). Adapted with permission.[138] Copyright 2018, Springer Nature. b) Timing scheme of presynaptic and postsynaptic spike applied to the two-terminal memristive device, the voltage differences lead to the device conductance modulation. Adapted with permission.[139] Copyright 2018, Springer Nature. c) Emulation of spike-timing-dependent plasticity using a redox-based memristive device. Adapted with permission.[67] Copyright 2015, American Chemical Society. d) Filamentary type, where the conductive nanofilament short circuits the cell. e) Volume type switching—here the conductivity of the whole volume is changed. f) Surface area type—the resistance change is area dependent, but only the interface resistance is modified.

neuron with memristive device, a fully memristive artificial neural networks was demonstrated for pattern classification.[129]

In biological neural networks, the neurons are connected by numerous synapses and dendrites. The input signals in presynaptic neuron are integrated as a function of time. An action potential (spike) is generated (fired) and subsequently transmitted to presynaptic neuron when the membrane potential reaches a threshold potential. After the firing process, the membrane potential is reset to resting potential (see Figure 2b). Various neuron models, such as leaky integrate-and-fire (LIF),[130,131] exponential integrate-and-fire (EIF),[132] adaptive exponential integrate-and-fire (AdEx)[133–135] and generalized exponential integrate-and-fire (GEM)[136,137] models have been developed to describe neuronal activities. In a standard leaky integrate-and-fire neuron model, the differential equation for membrane potential is given by:

$$\tau_{\mathrm{m}} \frac{d\Delta\varphi}{dt} = -\left(\Delta\varphi_t - \Delta\varphi_{\mathrm{rest}}\right) + \frac{I_{\mathrm{t}}}{G_{\mathrm{L}}} \tag{20}$$

where τ_{m} is the membrane time constant, $\Delta\varphi_{\mathrm{t}}$ is the membrane potential, $\Delta\varphi_{\mathrm{rest}}$ is the rest potential, I_{t} is the external input current, G_L is the membrane leakage conductance. In exponential integrate-and-fire neuron model, there exists an exponential dependence of $\Delta\varphi_t$ on the right side of Equation 20, implying the active potential generation is exponential, given by the differential equation:

$$\tau_{\mathrm{m}} \frac{d\Delta\varphi}{dt} = -\left(\Delta\varphi_{\mathrm{t}} - \Delta\varphi_{\mathrm{rest}}\right) + \Delta_T \exp\left(\frac{\Delta\varphi_t - \Delta\varphi_{\mathrm{th}}}{\Delta_T}\right) + \frac{I_{\mathrm{t}}}{G_{\mathrm{L}}} \tag{21}$$

where Δ_T is the nonlinearity of active potential initiation, $\Delta\varphi_{\mathrm{th}}$ is the effective threshold potential of the neuron. 2D neuron models such as adaptive exponential integrate-and-fire[133–135] and generalized exponential integrate-and-fire models[136,137] where the exponential nonlinearity is combined with a second current adaption variable have also been introduced to simulate neuron activities, especially to simulate various type of action potential signals. The models introduced above can be fitted to the Hodgkin–Huxley model, as introduced in Section 2, and provide effective and accurate descriptions about the timing of action potential firing in neuronal networks.

3.2. Electrochemical Artificial Synapses

Memristive devices can also act as synapses (**Figure 8**a) by changing the resistance between the electrodes.[138] In their basic operation principles, ReRAM synapses are closer rather to the electrical biological synapses (Figure 4b), than to chemical ones. The resistance change is reached either by forming/dissolving filaments, by incorporating/extracting donors/acceptors, or by forming/dissolving interfacial layers (Figure 8d–f). Same functions such as short- and long-term potentiation/depression, plasticity etc., as for biological synapses are also characteristic for electrochemical memristive devices. By gradually or abruptly change the conductivity (respectively resistance) of the device one changes the synaptic weights and can switch between non-volatile learning (memory) or adapt to learning/forgetting processes with different level and/or speed of forgetting and

learning. This enables the possibility of using memristive devices as artificial synapses for implementing spike-timing-dependent plasticity learning rule. The timing scheme of the applied voltage spikes (Figure 8b) can determine the conductance modulation of a memristive device.[139] This phenomenon is like the spike-timing-dependent plasticity, which describes the biological synaptic weight modulation is a function of the time difference presynaptic and postsynaptic spikes (Figure 5). Figure 8c shows the experimental measured conductance tuning in a memristive device. Long-term potentiation and long-term depression induced by the timing difference of voltage pulses.

The reported different switching mechanisms can in some sense be considered as representing different synapses, as the properties and stability of the device' resistances vary, depending not only on the material systems but also on the switching type. Also, in this case the properties of the synapses can be modified and even designed based on the selected materials systems, i.e., electrode materials and the type/composition of the solid electrolyte. For example, it has been found that Ag filaments in SiO_2 are formed faster but are less stable compared to Cu filaments in same matrix. Moreover, it is demonstrated that the dynamics of the metallic filament could be tuned by electrochemical alloying approach. Yeon et al.[106] reported that in amorphous silicon, Ag-Cu alloying conducting channels show enhanced reliability in contrast to Ag–Ti, Ag–Cr or Ag–Ni alloyed devices. Superior electrical stability and analog switching behaviors with low device-to-device variation were obtained in the Ag–Cu alloyed memristors.

It is also demonstrated that introducing doping into the matrix can accelerate or slow down diffusion, respectively tune the switching time and filament stability.[140] If the inserted doping is forming stronger bonds to the matrix the transport is retarded, but the stability of the formed filament is increased. In case of week bonding, the migration/switching is faster, but the filament is less stable. Factors, that can influence the cell resistance and state stability are also considered moisture/protons, excess ions from the active metal electrode, light illumination, and temperature.[141–144]

Memristive devices offer the unique possibility to be able to serve as both neurons and synapses. These properties are often used for different applications, including connecting biological and artificial neurons. The choice of the materials system and mobile species are a powerful tool for designing neural and synaptic properties on demand.

4. Synaptic Arrays and Applications

The previously mentioned artificial synapses and neurons serve as fundamental components (basic units) for neuromorphic systems. To create hardware neural networks using memristors, it is necessary to incorporate memristive arrays, particularly in a crossbar configuration, as this allows for optimal integration density and parallel computing capabilities. These arrays have gained significant attention in recent years due to their potential to improve the efficiency and performance of various applications. Memristor arrays offer a promising alternative to traditional computing architectures, particularly in applications such as artificial neural network acceleration and biological signal processing. In this section, we provide an overview of the current state of the neuron and synaptic arrays and applications, including a discussion of two-terminal and three–terminal arrays, their advantages and limitations, and recent research advancements. We also highlight the potential applications of these arrays in various fields and discuss the challenges and opportunities in the development and implementation of memristive-based neural systems.

4.1. Artificial Neurons and Synapses on a Single Device Level

4.1.1. Artificial Neuron Device

The leaky-integrate-fire (LIF) neuron model was developed based on the requirement that neurons surpass a specific threshold potential to trigger action potentials. This model solely describes the process of generating action potentials and excludes ion dynamics.[145] It is widely used in the field of neuromorphic computing due to its simplicity. Consequently, constructing LIF neurons with innovative principle devices is appealing as they offer high scalability and efficiency.

To implement LIF neurons on hardware, three crucial elements are leakage, accumulation, and emission. Leakage can be modeled by the relaxation process of devices, such as the heat dissipation of Mott devices[121,146,147] and ion diffusion in diffused memristors.[129] Leakage dynamics is fundamental for spatiotemporal integration and nonlinear computation of neuronal signals. Nonlinear physical processes of memristors enable the realization of cumulative properties, like heat accumulation in Mott devices[147,148] and the formation of conductive filaments in metal ion-based memristors.[129] Action potentials are triggered by strongly nonlinear transition processes in memristors, resulting in a sudden increase in device conductance, such as in Mott devices,[121,146,147] diffusion memristors,[129] and phase change memristor.[113]

The function of LIF neuron has been realized using diffusive memristors,[112,120,129] Mott devices[120] and phase change memristor.[113] Duan et al.[149] proposed compact implementation of LIF neuron using a NbO_x-based Mott device as shown in **Figure 9**a. such single neuron can perform nonlinear calculations, like signal gain modulation.

Neural oscillations refer to the repetitive or rhythmic neuronal activities in the biological nervous system that play a crucial role in brain functions such as feature binding and frequency-based information transmission mechanisms.[150,151] Thus, emulating oscillatory neurons on hardware is essential in developing neuromorphic intelligent hardware systems.

Currently, as depicted in Figure 9b, an effective approach to achieving oscillatory neurons involves connecting a Mott memristor[146] or an Ag-based ECM memristor in series with a load resistor.[152,153] By applying a long voltage bias as input, oscillating neurons can be realized and the firing frequency can be adjusted by varying the amplitude of the input pulse or the resistance value of the series resistance.[153] Furthermore, oscillatory neurons can be used to build a coupled oscillatory neural network, thereby expanding the range of potential applications for such neurons.

The H–H neuron model[83] is considered the most intricate and precise neuron model for describing the electrochemical processes of biological neurons. This model can accurately exhibit

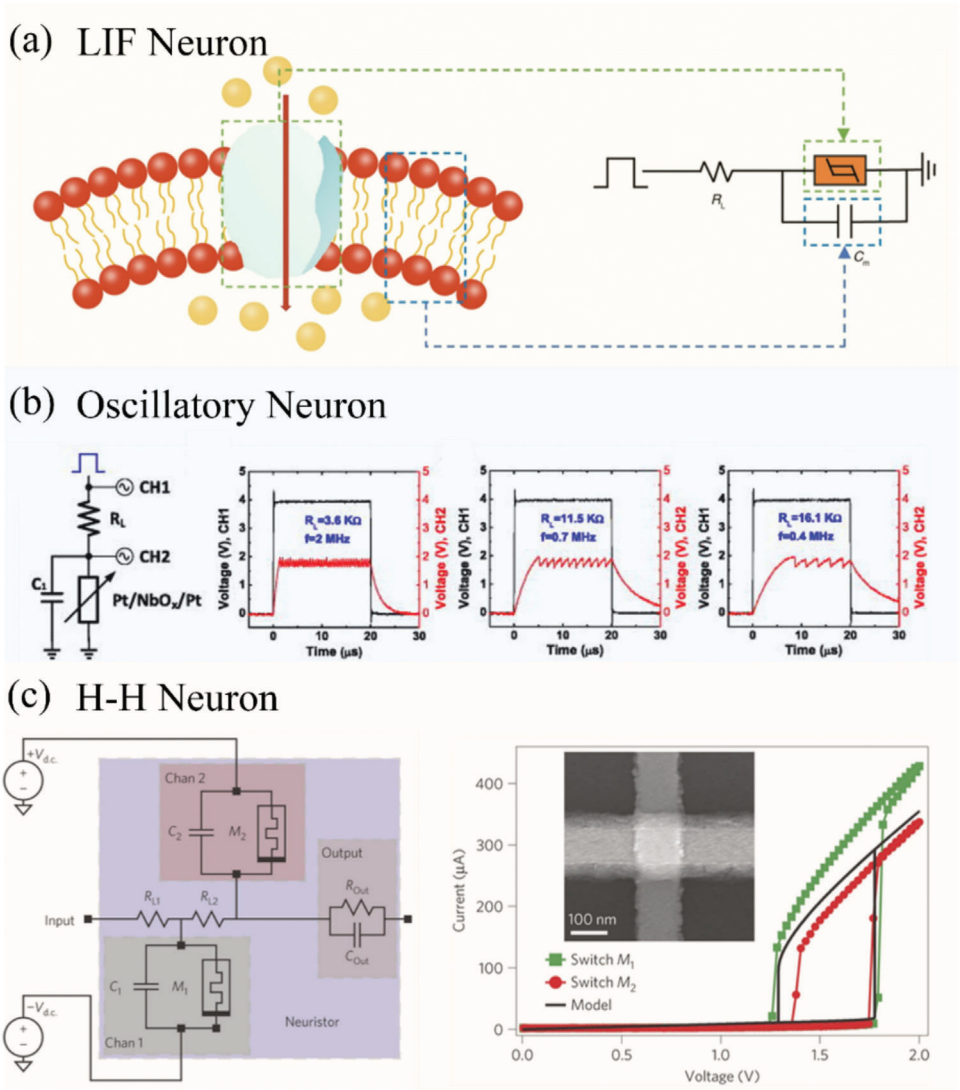

Figure 9. Implementation of artificial neurons using memristive devices: a) LIF neuron; b) oscillatory neuron; c) H–H neuron. a) Adapted with permission.[149] Copyright 2020, Springer Nature. b) Adapted with permission.[146] Copyright 2017, AIP Publishing. c) Adapted with permission.[147] Copyright 2013, Springer Nature.

various firing behaviors of biological neurons. It is a continuous model that comprises differential equations describing the conductance of each ion channel on the cell membrane. It is commonly used for studying the firing behavior and characteristics of individual neurons.

Pickett et al.[147] and Lin et al.[148] developed H–H neuron circuits using NbO_2 memristors as shown in Figure 9c. Two of the NbO_2 memristors have a shunt capacitor powered by a DC source of the opposite polarity to simulate the opening and closing of Na^+- and K^+-ion channels in the model. This circuit can replicate complex neuronal dynamics, such as all-or-nothing pulses, bifurcation thresholds, signal gain, and the refractory period of continuous pulse firing states. Furthermore, in 2018, Yi et al.[121] integrated the same circuit with VO_2 memristors to create H–H neurons that can produce 23 different types of neuron firing behaviors by adjusting the input signal, parallel capacitance, and series resistance. This system can achieve rich neuron behaviors based on the H–H neuron model and improve the prospects of bionic applications with raised hardware costs and operational complexity.

4.1.2. Artificial Synapse Device

In biological systems, neurons are interconnected through synapses, which can transmit signals in the form of electrical or chemical impulses from one neuron to another. The strength of these connections, described by synaptic weights, is not fixed and can undergo plasticity in response to various stimuli. Synaptic plasticity underlies both short-term and long-term learning in humans, making the development of artificial electronic synapses a crucial step in creating artificial systems. Recent advances in electronic synapse devices have shown great potential for realizing this goal. These devices include resistive

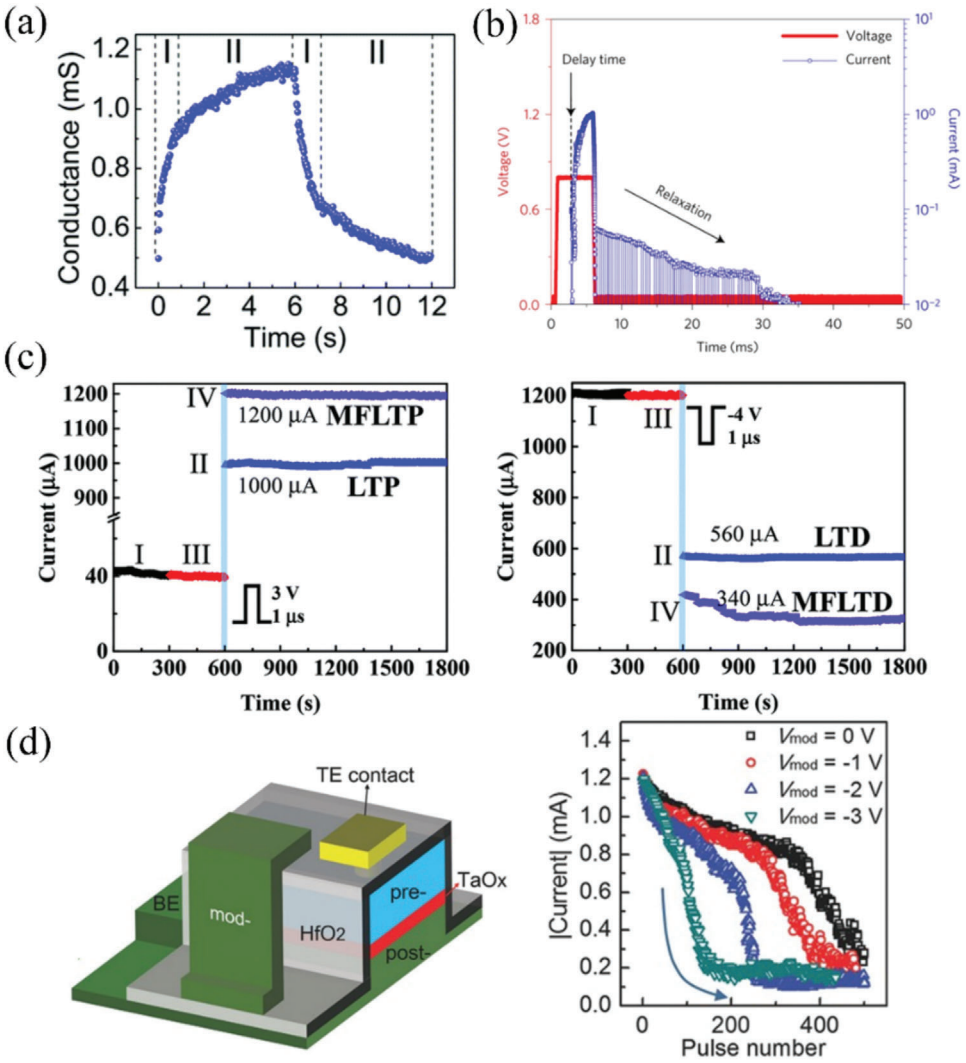

Figure 10. Various plasticity implemented by memristive devices: a) long-term plasticity (LTP); b) short-term plasticity; c) metaplasticity; d) heterosynaptic plasticity. a) Adapted with permission.[155] Copyright 2016, Royal Society of Chemistry. b) Adapted with permission.[58] Copyright 2017, Springer Nature. c) Adapted with permission.[156] Copyright 2018, Royal Society of Chemistry. d) Adapted with permission.[66] Copyright 2017, Wiley-VCH.

random-access memory, ferroelectric tunnel junctions, phase-change memory, magnetic memory, ferroelectric field-effect transistors, ion-gated transistors, floating-gate transistors, and charge-capture transistors.

In the 1980s, scientists first discovered long-term synaptic plasticity, which refers to the ability of the connection strength (weight) between neurons to change durably in response to stimulation of the presynaptic neuron and the postsynaptic neuron. In order to simulate the long-term plasticity of biological synapses, artificial synapses should be capable of non-volatile enhancement (inhibition) under external electrical stimulation. Long-term potentiation and long-term depression have been demonstrated in electrochemical metallization memory (ECM).[106] based on metal conductive filament and valence change memory (VCM) based on oxygen vacancy conductive filament.[154]

TaO_x[155] and HfO_x[154] resistive switching memories have also been reported to exhibit LTP/LTD characteristics. However, the LTP/LTD behavior of these devices generally exhibits nonlinearity, which can be improved by optimizing the device structure. Wang et al.[155] proposed inserting a SiO_2 layer as a diffusion limiting layer (DLL) between TiN and TaO_x to limit the number of oxygen vacancies involved in forming the conductive filament during the abrupt change process of LTP/LTD. This improves the linearity of the device as shown in **Figure 10**a. Jo et al.[63] developed Ag:Si/Si ECM memory and demonstrated LTP/LTD characteristics using this device. However, the retention and uniformity of ECM devices can still be improved. Yeon et al.[106] proposed using Ag–Cu alloy as the active electrode for ECM devices in which the conductive filament is more stable.

Short-term plasticity refers to the phenomenon of synaptic weight changes within a short time scale of milliseconds to minutes, including short-term potentiation (STP) and short-term depression (STD).[157] Artificial synaptic devices with short-term characteristics can be constructed using short-term physical processes in devices. For example, Wang et al.[58] achieved STP, STD,

and other short-term plasticity in ECM resistive switching devices based on Ag conductive filaments, as shown in Figure 10b. Under weak pulse stimulation, weaker Ag conductive filaments were formed in the device, and the poor stability of the larger surface energy of Ag caused the filaments to gradually dissolve after the stimulation was removed, resulting in short-term effects in the device.

Metaplasticity is an important concept in synaptic plasticity research, as it refers to how the history of a synapse's activity can affect its current plasticity. This can be understood as the plasticity of synaptic plasticity.[158] Wu et al.[156] studied different types of resistive switching devices and found that by applying a small pulse to the device, which does not significantly change the device's conductivity but affects the state of the conductive filaments, the LTP/LTD produced by the second pulse is stronger/weaker than that produced without the small pulse, as shown in Figure 10c.

Heterosynaptic plasticity is a phenomenon where specific synaptic pathways can undergo weight changes without direct stimulation.[159] There are various forms and mechanisms of heterosynaptic plasticity, with one widely studied phenomenon being the modulation of synaptic plasticity by the release of modulatory neurotransmitters from a third neuron. Device-based heterosynaptic plasticity utilizes the effect of the third terminal's field-effect and electric field on ion migration. Yang et al.[66] fabricated a vertically structured Ta/TaO_x three-terminal memristor, as shown in Figure 10d. Applying a voltage between the top and bottom electrodes causes oxygen vacancy conductive filaments to form in the device, and applying a voltage to the sidewall modulation electrode can adjust the electric field distribution in the resistive layer, thereby affecting the formation of conductive filaments. When different voltages are applied to the third terminal, the Set/Reset voltage and LTP/LTD characteristics of the device can be modulated.

4.2. Two-Terminal Memristor Array

Two-terminal memristors are passive electronic devices that exhibit resistance transition based on the history of the current passing through them. These memristors can be integrated into a crossbar array structure, which allows high degree of parallelism and computational efficiency for the implementation of various memory and computing functions.

Passive memristor array and CMOS–memristor hybrid array are two types of memristive integration methods that are commonly used. A passive memristor array, also known as a memristive crossbar array, consists of an array of memristors arranged in a crossbar configuration. The passive memristor array is capable of performing various analog and digital computing operations with high integrate density. In contrast, CMOS–memristor hybrid array consists of a transistor and memristor. This structure provides an opportunity for fabricating a larger array and supporting more complex applications.[45,160–164]

4.2.1. Passive Memristor Array

One of the key advantages of the passive memristor array is its simplicity, as it only requires a single layer of memristors arranged in a crossbar configuration (**Figure 11**a). However, it has limited read and write capability due to the sneak path problem as shown in Figure 11b, which can cause crosstalk involving a series of memristors. This issue gets worse as the array size grows, thus limiting the size of passive memristor arrays.

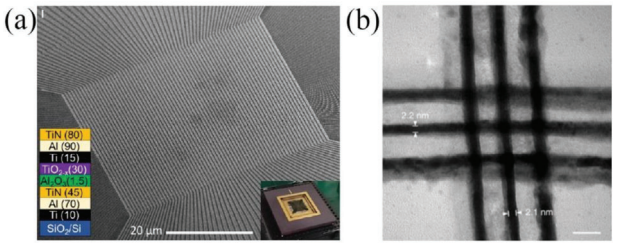

Figure 11. a) Scanning electron microscopy (SEM) images of patterned 4K memristor analog passive crossbar array. Adapted with permission.[165] Copyright 2021, Springer Nature. b) TEM image of a 3 × 3 memristor crossbar array with 2 × 2 nm^2 device area and with sub-12 nm pitch. Adapted with permission.[166] Copyright 2019, Springer Nature.

A 4K memristor analog passive crossbar array was reported[165] using Ti/Al/TiN/Al_2O_3/TiO_{2-x}/Ti/Al/TiN devices, with 99% functional nonvolatile metal-oxide memristors as shown in Figure 11a. To achieve better uniformity for the devices in the main array, an additional line is added at both sides of the circuit for the top and bottom layers forming dummy cells. In order to increase the integration density, another effective technical route is to reduce the feature size of the device, Pi et al.[166] demonstrate memristor crossbar arrays with a 2 nm feature size and a single layer density up to 4.5 terabits per square inch as shown in Figure 11b. Such extremely small functional memristors provide a power efficient solution for information storage and processing.

As technology continues to advance, there is a growing need for more powerful and efficient computing systems. with the increasing demand for more processing units, which leads to research shift towards 3D crossbar arrays. The transition from 2D to 3D crossbar arrays involves a significant increase in complexity as additional layers must be added to enable the processing of more inputs and outputs. This structure allows for an exponential increase in the number of connections that can be made, resulting in a significant increase in processing capability However, this increased complexity also presents challenges, such as the need for more precise manufacturing.

There are 3D horizontally integrated array and 3D vertical integrated array basically. In 3D horizontal integrated array architecture, the density of memristors is increased by vertically stacking 2D arrays. Adam et al.[167] reported monolithically integrated 3D metal-oxide memristor crossbar with two passive 10 × 10 Pt/Al_2O_3/TiO_{2-x}/TiN/Pt memristor crossbars with shared middle electrodes as shown in **Figure 12**a. The equivalent circuit shown here depicts two memristors arranged in a stacked configuration with that the middle electrode is shared by both the bottom and top devices. To reduce the likelihood of shorts and large variations caused by the high step height, a planarization step was performed prior to depositing the top layer of active metal. Consequently, the electrical behavior of both the bottom and top crossbar layers is similar, and the device-to-device uniformity is satisfactory.

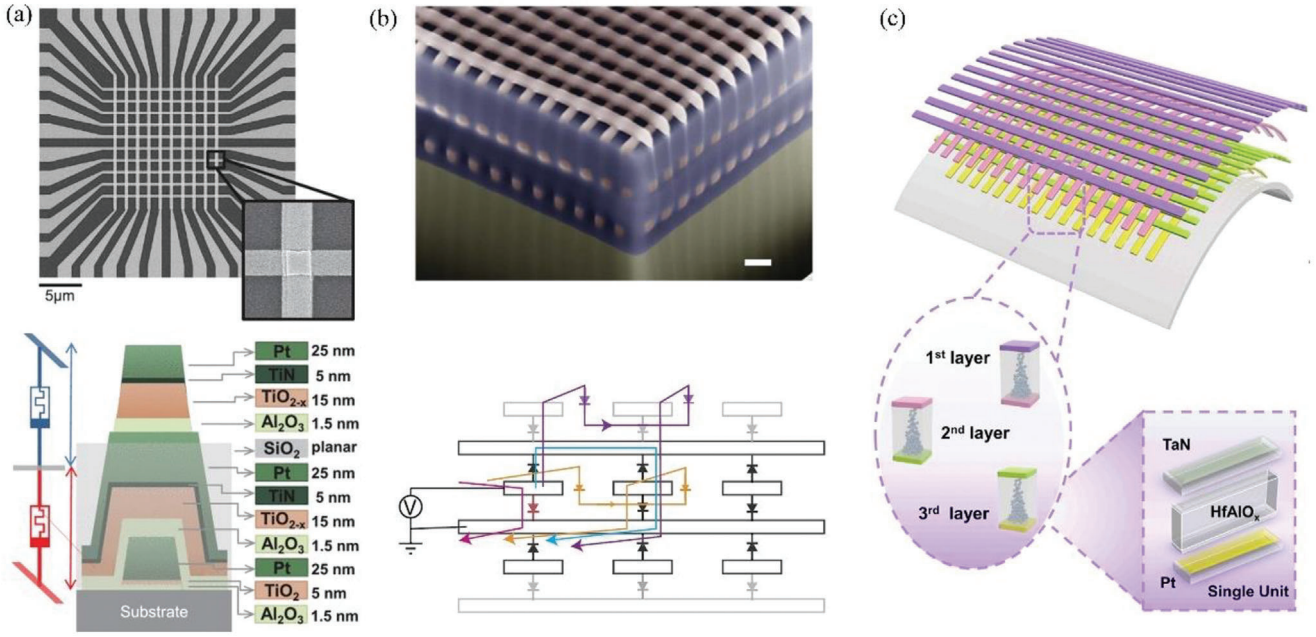

Figure 12. a) Scanning electron microscopy top-view image of the fabricated memristor array and equivalent circuit for two memristors in the stacked configuration. Adapted with permission.[167] Copyright 2017, IEEE. b) Horizontally integrated 3D crossbar array with isolation between different layers and the schematic representation for 3D stacking with shared electrodes between adjacent layers. Adapted with permission.[168] Copyright 2017, Springer Nature. c) Schematic of 3D crossbar memristors array consisting of first, second and third-layer memory units (Pt/$HfAlO_x$/TaN). Adapted with permission.[169] Copyright 2021, Wiley-VCH

With more layer integrated on horizontal, the sneak path issue becomes prominent challenges that leads to operational failure and high power consumption.[73] To address this issue, 3D all-silicon-based memristor array with built-in rectifying selector is built using a p-Si/SiO_2/n-Si structure as shown in Figure 12b.[168] The interlayer sneak path is illustrated by the blue curve, while the intralayer sneak path is represented by the orange curve. A sneak path that extends beyond one layer and is positioned on top of a selected layer, as depicted by the purple line, will necessarily traverse at least 3 reverse biased devices, thereby limiting the current in the sneak path. This work experimentally confirmed the successful suppression of both intra- and interlayer sneak path currents through the built-in diodes.

Also, the flexible 3D memristive array is developed via low-temperature atomic layer deposition on the flexible substrate as shown in Figure 12c.[169] The typical bipolar switching characteristics are verified in memrsitor units of 3D network, including three layers.

Unlike 3D horizontally integrated array, 3D vertically integrated array utilizes pillar electrode to serve as WL and the switching layer was deposited on the sidewall. as shown in **Figure 13**a. A technology path that is cost-effective for 3D integration and requires only one critical lithography step or mask to reduce the cost per bit is demonstrated.[170] The process of atomic layer deposition is used to deposit a thin film of HfO_x on the sidewall of a pre-defined trench, creating a vertical memory structure. By engineering the interface between the electrode and the oxide layer using a TiON interfacial layer, a non-linear *I*–*V* response is achieved, making it suitable for a selector-less array. Figure 13b–f show the detailed structure of this implementation.

In order to integrate more devices to further increase the integration density, a 3D vertically integrated array with 8 layers was fabricated as shown in Figure 13g,h. Pillar electrode is extracted by sputtering the TiN/W to fill the hole and each horizontal BL was opened by selective etching successively.[39] The sidewall of each cell in the device shows interface type behavior that differs from the conductive filaments. This results in a uniform distribution of the device and allows for continuous modulation of resistance. The resistance can be modulated by changing the barrier between the electrode and the dielectric material or by inducing charge capture/release through defects in the material body.

The current sidewall-integrated vertical memristive architecture offers an economical way to achieve multilevel functionality, but it has only been demonstrated in small size arrays. Moreover, the scalability of this approach to larger layers may be limited by the high aspect ratios required during deposition of pillar electrode,[171] or the low current drivability of the vertical selector.[172]

In the 3D integrated array, thermal effects present a significant challenge during both the fabrication and operation of multilayer systems.[173,174] In order to preserve the material properties of previously fabricated layers, a low temperature budget is necessary during fabrication. High temperatures during deposition or photoresist baking may lead to interlayer diffusion, which reduces control over dopant concentration and nonstoichiometry. Additionally, the switching mechanism for most metal-oxide memristors involves significant Joule heating, which can cause High temperatures.[175] Such high temperatures can disrupt the state of neighboring devices separated only by a thin middle electrode. A recent theoretical study[176] has suggested that thermal

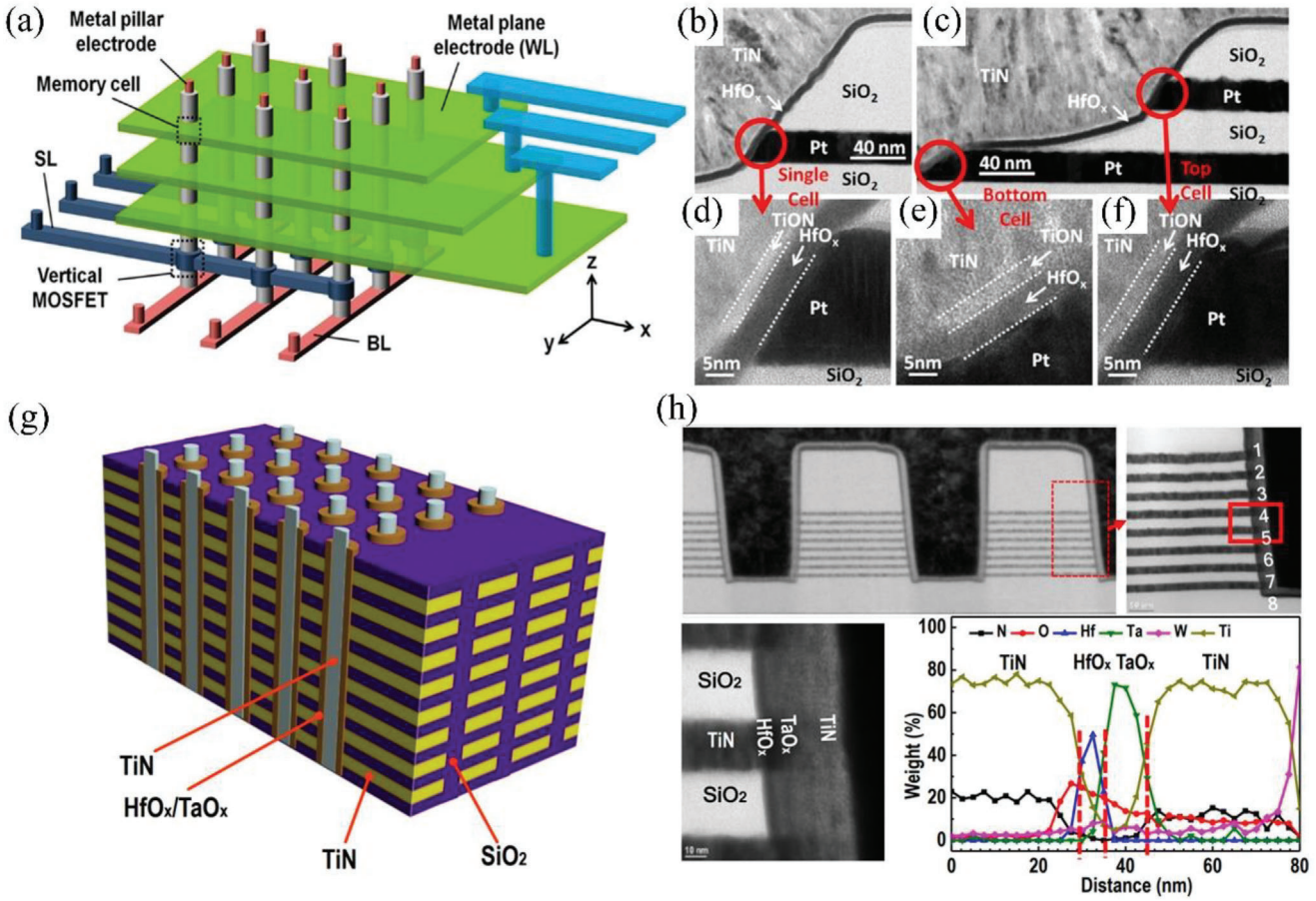

Figure 13. a) Schematic of the 3D vertically integrated array using the vertical memristor cell, the vertical memristors are formed at the intersections of each pillar electrode and plane electrode. Adapted with permission.[170] Copyright 2013, American Chemical Society. b–f) Cross-sectional TEM of single-layer sample and double-layer sample. b–f) Adapted with permission.[170] Copyright 2013, American Chemical Society. g) 3D vertically integrated array with 8 layers. h) Corresponding TEM image of the eight-layer stacks (g) with EDS mapping. g,h) Reproduced with permission.[39]Copyright 2022, Springer Nature.

crosstalk in 3D integrated array can cause device performance degradation and failures, particularly during the power-intensive reset step.

4.2.2. CMOS–Memristor Hybrid Array

Different with passive memristor array, CMOS–memristor hybrid array can overcome the sneak path problem by using transistor to isolate the memristor, enabling precise read and write operations.

Memristive devices offer several benefits, such as their compact size, typically on the order of $4F^2$, where F represents the lithographic feature size or half-pitch. Additionally, they have simple structures that are easily fabricated and integrated with conventional CMOS processes. However, it is worth noting that memristive devices are not active components, unlike CMOS transistors, as they are unable to supply energy to a circuit. To address this issue, a possible solution is to combine crossbar arrays of memristive devices with a conventional CMOS layer that provides signal restoration and gain, albeit at a much lower density. This approach, known as CMOL (CMOS molecular-scale devices), was initially proposed within the context of nonphotolithographic techniques.

Strukov et al proposed a topological structure based on CMOL architecture that offers an uncomplicated yet effective design for building and utilizing crossbar arrays.[177] As shown in **Figure 14**a, this design enables the integration of memristive crosspoint devices at a higher density than the lateral feature sizes typically allow, thus exceeding scaling limits. Figure 14b shows the 3D hybrid CMOS/crossbar circuit. The wire and via patterns are uniform across all crossbar layers, ensuring consistent area density of vias throughout the stacked layers.[177] This means that adding new layers does not necessitate modifications to the underlying layers, making this crossbar layer stacking scheme highly cost-effective.

Besides the significant advantages in terms of integration, the mainstream solution is to adopt the 1T1R pseudo cross-array structure, which can suppress the sneak path through transistors when accessing a single device. And turn on selected transistors at the same time when parallel computing is required, so as to obtain the same parallelism advantage as the passive cross-array

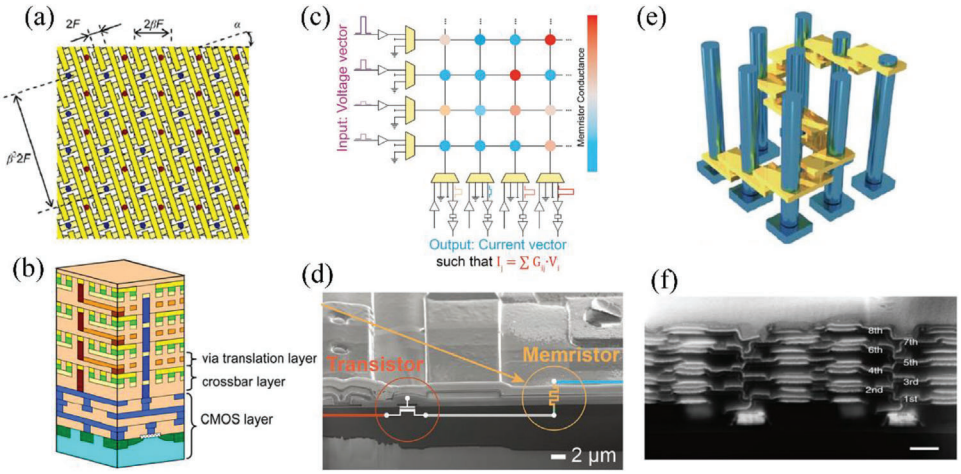

Figure 14. a) Top view of the crossbar (top) layer. b) Cut-away illustration of the circuit showing four crossbar layers. Adapted with permission.[177] Copyright 2009, National Academy of Sciences, USA. c) Schematic showing the implementation of vector-matrix multiplication using memristor crossbar devices. Adapted with permission.[163] Copyright 2018, Wiley-VCH. d) Memristor device fabrication and processing integration for the 1T1M memristor array. Adapted with permission.[178]Copyright 2018, Springer Nature. e) Schematic of one kernel of CNN presented by staircase memristor array. f) Cross-sectional view of the staircase memristor array. e,f) Adapted with permission.[179] Copyright 2020, Springer Nature.

structure. As shown in Figure 14c, the desired vector is converted into applied voltages (shown in purple) along the rows, and the resulting current collected from each column produces the VMM (vector-matrix multiplication) of the memristor conductance matrix G_{ij} and voltage vector V_j.[163] The current from each column is collected by the transimpedance amplifier (TIA) and then converted into a voltage signal, which is stored by a sample and hold (S/H) circuit and sensed by an analog-to-digital converter (ADC). Each column can be configured to either measure current through the TIA, S/H, and ADC path, or apply voltages along the digital-to-analog converter (DAC) path. The fabrication and processing integration of memristor devices are crucial in creating a 1-transistor-1-memristor (1T1M) memristor array (Figure 14d).[178] Front-end-of-the-line (FEOL) CMOS transistors and 2 μm technology-based wiring form the base structure, enabling precise access to individual memristor cells during programming. A foundry-compatible back-end-of-the-line (BEOL) process integrates the Ta/HfO_x/Pd memristor layer on top of the CMOS. In a 1T1M array, the bottom electrode (BE) lines are shared between rows, while the top electrode (TE) lines and transistor gate lines are shared between columns. Isolation between the rows and columns is provided by the interlayer dielectric (ILD).

The highly complex connections in a convolutional neural network (CNN) would inevitably require complex 3D structured back-end-of-line interconnects between 2D arrays. A 3D circuit composed of eight layers of monolithically integrated memristive devices.[179] As shown in Figure 14e,f, the vertically aligned input and output electrodes in the 3D structure make it possible to directly map and implement complex neural networks which provide highly compact and efficient implementations of CNNs.

Overall, both passive memristor array and CMOS–memristor hybrid array are important components in memristive circuits, each with its own advantages and disadvantages. The choice of which array to use depends on the specific application requirements and design considerations.

4.3. Three Terminal Memristor Array

Electrochemical memristor, or electrochemical random-access memory (ECRAM), has been extensively researched as an analog synaptic device for implementing ideal synaptic features such as symmetric potentiation and depression based on its switching mechanism or material properties.[180–182] Studies have shown that ECRAM exhibits excellent synaptic characteristics and high performance, including programming times comparable to memory-class devices at 10 nanoseconds and low programming energy levels down to approximately 10^{-4} Joules per second.[183] This owing to their nondestructive-weight-update behavior, which is attributed to the completely separated terminals for reading and writing.[17,184–188]

However, when it comes to complex circuit configurations, three-terminal synapses have some drawbacks compared to the two-terminal crossbar array structure. Specifically, they have a lower array density and are limited in their line-design structure, which ultimately leads to lower processing speeds and higher energy consumption for the entire system.

A vertical synapse featuring a remote weight update via ion gel was proposed to extend three terminal memristor to a crossbar array structure.[189] In the proposed ion-gel-gated artificial synapse, p-type P3HT was used as the vertical channel, whereas an ion-gel consisting of ionic liquid and poly(vinylidene fluoride-co-hexafluoropropylene) (PVdFHFP) was used as the gate dielectric layer. As shown in **Figure 15**a,b, A poly(3-hexylthiophene) (P3HT) channel with a thickness of less than 100 nm is situated at each crosspoint of the pre- and postsynaptic terminals, with the ion-gel weight-control layer being applied onto them. The mobile ions present in the ion gel can easily permeate the unoccupied space within the P3HT channel, leading to an enduring alteration in the channel's conductance. This feature holds crucial significance for synaptic properties.[189]

Three-terminal memristive devices can be integrated through stacked and sidewall structures. A new type of ECRAM, called

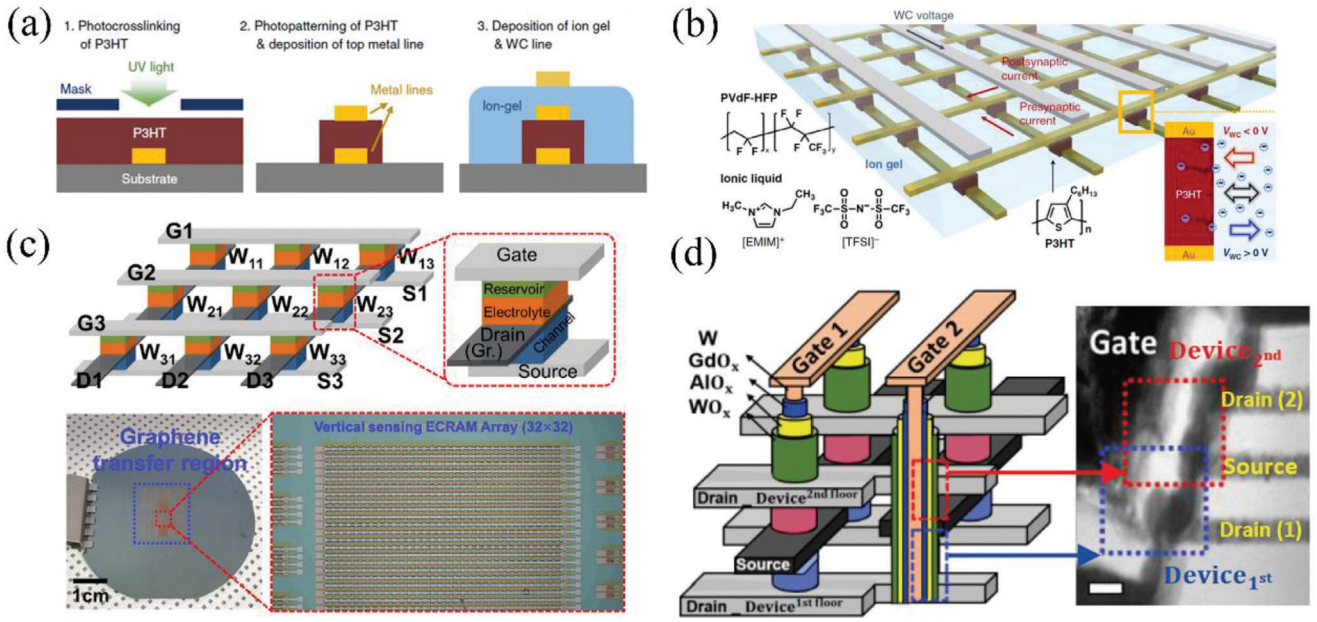

Figure 15. a) Cross-sectional schematic of fabrication procedure of ion-gel-gated vertical P3HT synapse. b) Schematic diagram of ion-gel-gated vertical crossbar synapse array mimicking biological NN. The inset shows the chemical structures of P3HT, PVdF-HFP, and ionic liquid. a,b) Adapted with permission.[189] Copyright 2020, Springer Nature. c) A 32 × 32 size VS-ECRAM array fabricated on a 2 inch SiO_2/Si wafer. Adapted with permission.[190] Copyright 2022, IEEE. d) Schematic illustration of the stacked 2 × 2 arrays comprising vertical STs and cross-sectional TEM image of experimentally stacked pair of synaptic memristors. Adapted with permission.[191] Copyright 2021, The Japan Society of Applied Physics.

the vertical sensing ECRAM (VS-ECRAM),[190] which utilizes a novel structure to address the limitations of the conventional lateral ECRAM (LT-ECRAM) was proposed. As shown in Figure 15c, by using a monolayer graphene electrode to precisely control the injection of Li-ions, ideal weight-update linearity in the VS-ECRAM can be achieved. Additionally, the graphene electrode serves as a barrier to prevent ion mixing between the channel and the electrolyte, ensuring superior reliability properties. These exceptional synaptic characteristics were maintained even at a small scale of 30 × 30 nm^2, resulting in improved write and read energy efficiency. The vertical channel structure also eliminates the lateral diffusion term, enhancing the read latency. Sidewall structures have also been proposed as shown in Figure 15d.[191] The vertically structured exhibits excellent synaptic characteristics while maintaining a small device area of $4F^2$. Sidewall structures with a channel length of 50 nm exhibit a significant improvement (>10^3) in switching speed indicating potential to be a promising candidate for high-density synapse array applications.

4.4. Integration of Artificial Synaptic Array and Neuron

The integration of artificial synapse arrays and artificial neurons can fully exploit the advantages of memristive devices in terms of area and power consumption. However, due to the difficulties in the heterogeneous integration process and impedance matching, such attempts are quite challenging. Wang et al.[129] demonstrated the integration of memristors with diffusive neurons. An overview of the integrated chip, which includes a 1-transistor-1-memristor synaptic array and diffusive memristor neurons, is shown in **Figure 16**a. The synaptic connections were created by integrating diffusive and drift memristors with foundry-made transistor arrays using back-end-of-the-line (BEOL) processes. Duan et al.[149] monolithically integrated memristive system using passive synaptic array and IMT neuron. Pt/Ta/Ta_2O_5/Pt synaptic devices and NbO_x based neurons were fabricated together in hardware. Figure 16b provides SEM images that demonstrate the overall structure of a synapse crossbar array with NbO_x neurons located in each row. The structural configurations of both the NbO_x neurons and Pt/Ta/Ta_2O_5/Pt synapses were evaluated using cross-sectional high-resolution TEM. Pattern recognition via online learning using a simplified δ-rule and coincidence detection is presented using such system.

4.5. Application Based on Synaptic Array

Based on the Artificial neuron and synapse devices and arrays illustrated above, it is possible to construct neuromorphic computing systems. Memristor crossbars can accelerate the VMM operation due to the parallel, in-memory, and analog features of memristors, which can accelerate a wide range of neural networks. Additionally, utilizing switchable two-level device states could enable the development of logic systems capable of performing basic logic gate operation and logical cascade. Further, by combining the memristive system and biological system, it is possible to use memristors to process biological information. The majority of current studies are focused on memristor-based ANN accelerators, with only a few studies on other types of neuromorphic systems. Ionic memristors are considered highly promising device candidates and attract extensive research interest compared to other device technologies. Passive memristor arrays and

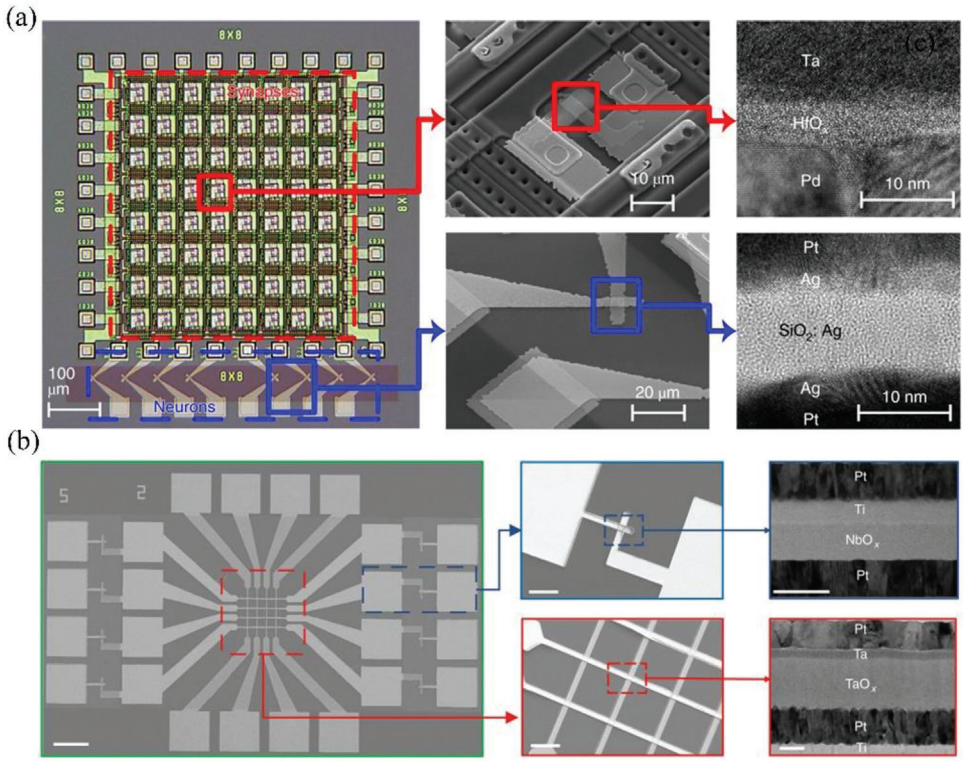

Figure 16. a) Overview of the integrated 1-transistor-1-memristor synaptic array and diffusive memristor neurons. Adapted with permission.[129] Copyright 2018, Springer Nature. b) SEM and TEM images of monolithically integrated memristive system using passive synaptic array and IMT neurons. Adapted with permission.[149] Copyright 2020, Springer Nature.

1-transistor-1-resistor (1T1R) arrays have been widely employed in existing studies. In this section, we discuss ANN accelerators based on memristors and will explore other logical operation accelerator and biological information processing systems enabled by memristor dynamics respectively.

4.5.1. Synaptic Array Based Neural Network Accelerator

It is widely known that single-layer perceptrons are only capable of solving linearly separable problems. However, this issue can be addressed by using perceptron networks with hidden layers. Recently, a multilayer perceptron network with one integrated hidden layer was reported, which consisted of two separated passive memristor crossbars corresponding to synaptic weights in different layers, as shown in **Figure 17**a.[192] The periphery circuits and neurons were implemented by discrete CMOS components. In addition to this multiple crossbar method, synaptic weights in different layers can also be realized by a large memristor array with proper partitioning. As shown in Figure 17b, a two-layer perceptron can be constructed by partitioning the monolithic 128 × 64 1T1R array.[193] This network can be trained online using the standard MNIST dataset and achieves high classification accuracy, demonstrating the potential of online learning to tolerate device imperfections.

Building 3D circuits using CMOS transistors in the standard CMOS process is a challenging task because the multilayer structure does not allow for the construction of a single-crystalline silicon channel. However, constructing 3D memristor circuits is more achievable since memristors are fabricated in metal layers. The memristor cells in the multilayer are stacked together, but this structure does not support 1T1R cells. Therefore, special techniques are required for fabricating and operating a single cell without interference.

The process of kernel sliding on an image requires a number of kernel VMM operations, which can be either time-consuming or require a large amount of area. However, a 3D memristor array provides a solution for conducting VMM operations with high parallelism and area density. To conduct a convolution kernel operation in a 2D memristor array, the 2D kernel or 2D input data must be unrolled into 1D vectors.

The demonstration of a 3D memristor circuit included eight layers of memristors,[179] as shown in Figure 17c,d. This 3D array supports efficient convolutional neural networks and video signal processing, with all convolution VMMs being performed in parallel. Once the image is input in 2D format, the convolution result can also be read out in 2D format, as shown in Figure 17e.

4.5.2. Memristor-Based Logical Operation and Logical Cascade

Memristor is an electrical component that exhibits resistive switching properties with a non-linear behavior. The switching can either be smooth or abrupt, depending on its physical characteristics. Essentially, a memristor retains its state without any external influence, meaning that it keeps its state after being

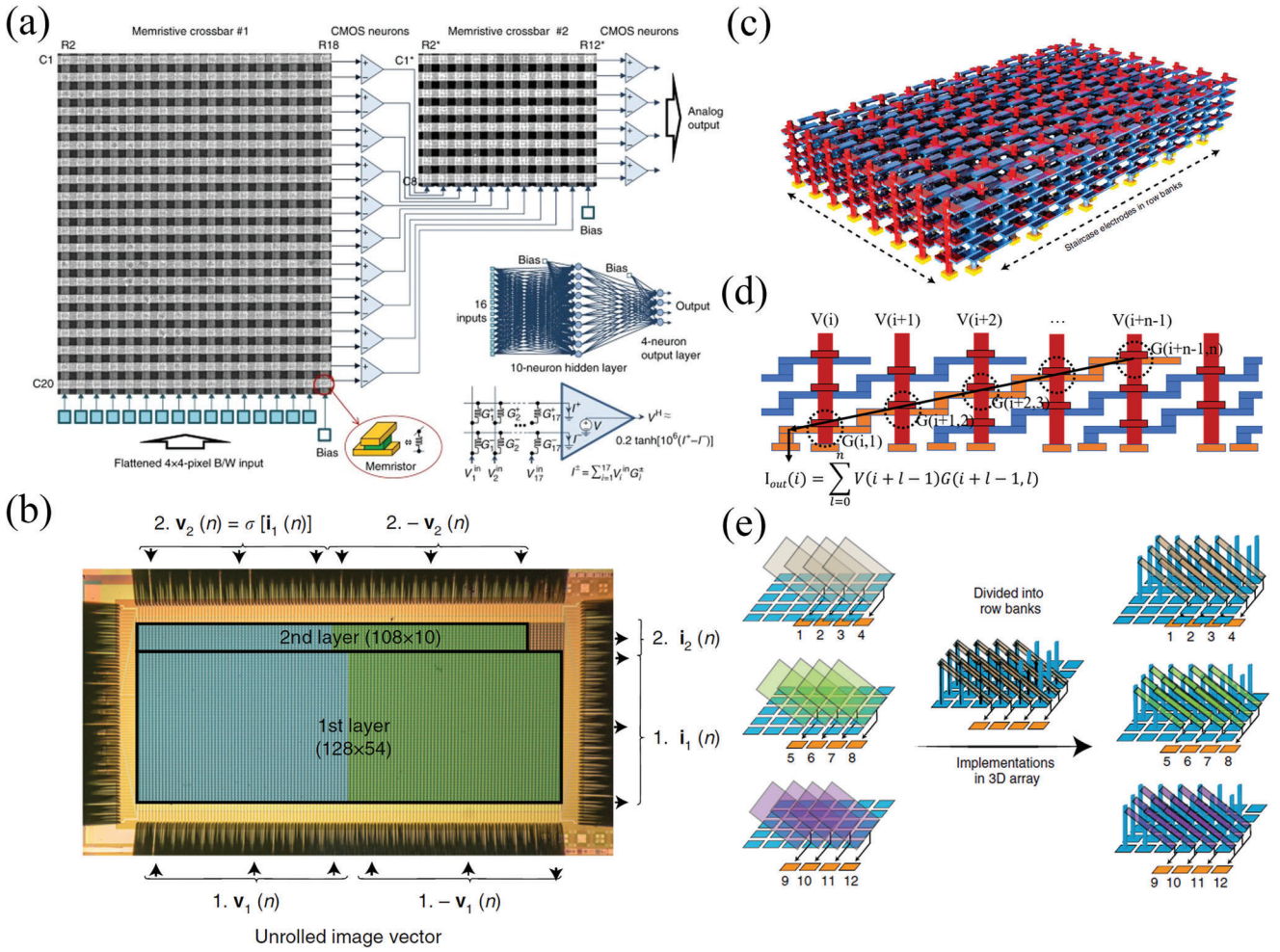

Figure 17. a) Multilayer perceptron classifier using two passive memristive crossbar arrays. Adapted with permission.[192] Copyright 2018, Springer Nature. b) Multilayer perceptron network based on partitioned CMOS–memristor hybrid array. Adapted with permission.[193] Copyright 2018, Springer Nature. c) 3D memristor architecture. d) Cross-sectional schematic of 3D memristor structure. The pillar electrodes (red) are used as input while the staircase electrodes are output. e) Paradigm of 2D convolution in 3D memristor array. c–e) Adapted with permission.[179] Copyright 2020, Springer Nature.

SET or RESET unless the voltage difference between its terminals falls within specific constraints. Due to this inherent feature, the memristor is suitable for logical operation which leads to in-memory computing. Memristor-based Snider Boolean Logic model was developed using model shown in **Figure 18**a. which considers lower resistance R_{ON} as logic 0 and higher resistance R_{OFF} as logic 1.[194] The logic synthesis process for a crossbar involves selecting which switches to activate and deactivate to implement a specified Boolean function. A memristor switch can be programmed to operate in two ranges: vertical lines indicate the minterms and inputs, respectively. If an input is present in the minterm, the corresponding switch is activated; otherwise, it is disabled. Results of logic mapping are shown in Figure 18b using crossbar with two levels.[194]

Figure 18c,d show hardware implementation of a logical unit using monolithic memtransistor technology based on 2D semiconductors of monolayer MoS_2.[195] As shown in Figure 18c, memtransistors are three-terminal devices where the gate terminal enables non-volatile and analog programming of conductance states, which can then be read by source-to-drain bias. An area and energy-efficient s-bit generator circuit composed of six memtransistors, which allows for a tunable probability of obtaining "1" in the bitstream over the range [0,1]. Moreover, s-bit generators with a 2D-memtransistor-based 2 × 1 MUX consisting of three NAND gates and one NOT gate, as shown in Figure 18d. The inherent stochasticity of charge trapping and detrapping processes in the gate dielectric of the memtransistor was exploited. This approach based on three-terminal 2D memtransistors not only overcomes the limitations of conventional digital CMOS but also eliminates the need for peripherals. The building blocks of NAND gates and s-bit generators can be cascaded to perform complex tasks.

4.5.3. Memristor Based Biological Information Processing Systems

The function of the brain depends on circuits of neurons that spike with synapses playing a crucial role in integrating

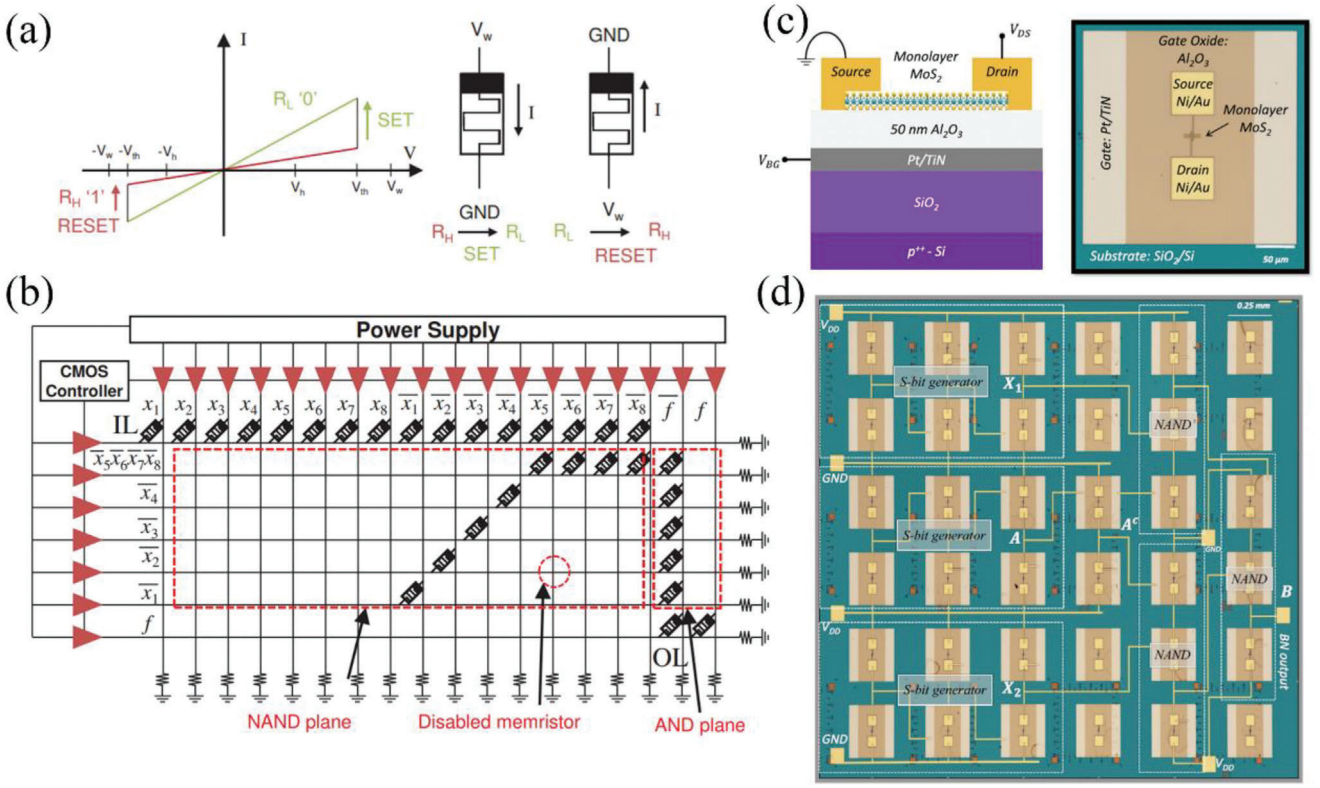

Figure 18. a) Illustration of the *I–V* characteristics and switching behavior of a required memristor. b) Logic mapping of a Boolean function on a crossbar with two levels. a,b) Adapted with permission.[194] Copyright 2018, IEEE. c) 2D schematic and optical image of 2D memtransistor based on monolayer MoS_2. d) 2-input NAND gates and s-bit generators based on 2D memtransistor. c,d) Adapted with permission.[195] Copyright 2022, Springer Nature.

transmission with memory storage and processing. Electronics have made significant strides in emulating neurons and synapses, and concepts related to brain–computer interfacing, which connect the brain with brain-inspired devices, are starting to become a reality. Serb et al have reported on memristive connections between the brain and silicon-spiking neurons that mimic the transmission and plasticity properties of real synapses.[196] A memristor combined with a thin film of titanium oxide microelectrode made of metal links a silicon neuron to a neuron in the rat hippocampus (**Figure 19**a). Memristive plasticity enables modulation of connection strength, while transmission occurs through weighted stimuli via the thin film oxide, resulting in responses that resemble excitatory postsynaptic potentials. The reverse link from the brain to silicon is created using a microelectrode–memristor pair.

Using Pt/TiO_x/Pt memristors in different configurations, the two synapses, ABsyn and BAsyn, connect the presynaptic silicon neuron (ANpre) to the brain neuron (BN), and BN to the postsynaptic silicon neuron, ANpost. The two memristors, MR1 and MR2, emulate plasticity in the two synapses, while the CME and the patch-clamp electrode mediate electronics-to-BN and BN-to-electronics signal transmission. With this structure, the ABsyn and BAsyn synapses respectively enable artificial-to-biological and biological-to-artificial communication by emulating two fundamental functions of biological synapses: signal transmission and plasticity-mediated signal processing.The operation scheme can be seen in Figure 19b.

Liu et al. demonstrated the use of memristor-based brain-machine interfaces for seizure detection.[160] **Figure 20**a,b illustrates their brain-machine interface concept and the system flow for detecting seizures. They employed memristor arrays to construct four FIR bandpass filters, dividing the input analog neuronal signal into four different frequencies: delta, theta, alpha, and beta. Biomarkers were then extracted from the filtered signal, and a memristor-based single-layer perceptron was used for classifying the brain state. They claimed that their memristor-based system achieved approximately 400 times power efficiency compared to traditional CMOS circuits, mainly due to processing analog signals directly in the analog domain and performing in-memory computations on memristor crossbars, which saves energy consumption of frequent memory access in traditional Von Neumann architecture. As proof-of-concept work, some segments of the whole system, such as biomarker extraction, were done in software. Li et al. proposed a parallel convolutional neural network using memristor arrays for seizure detection and prediction.[197] To compensate for the accuracy loss due to digital-analog conversion and non-idealities of memristor arrays, they adopted quantization-aware training and a weight-offsetting method. The proposed network includes fewer parameters but achieves comparable results to state-of-the-art methods. By paralleling the different convolutional kernels on separate memristor arrays, the proposed network's latency was reduced by two orders of magnitude compared to the previous memristive–CMOS architecture.

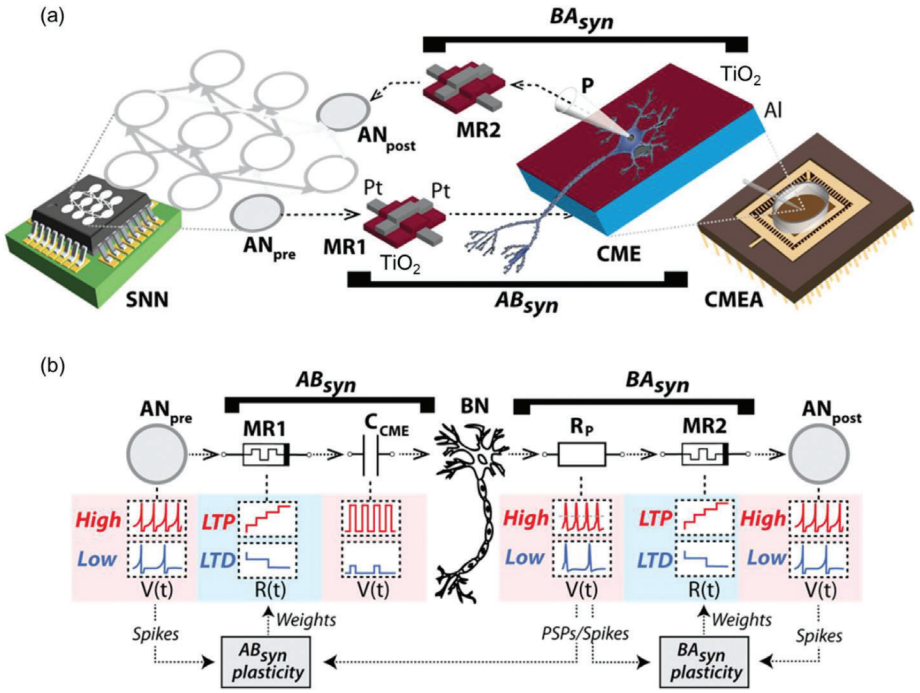

Figure 19. a) Sketch of the main components of the hybrid circuit and of the synaptors. b) The brain neurons hybrid network operational scheme. a,b) Adapted with permission.[196] Copyright 2020, Springer Nature.

Here, we provide an overview of memristive synapses array and application, as well as their respective advantages and disadvantages. We also discuss neural network and logic operation based on memristive crossbars, as well as biological information processing systems that link the memristors and biological system. Despite the promising progress made thus far, memristor-based neuromorphic systems are still in their early stages, and several outstanding challenges remain unresolved in current studies.

Considerable effort should be devoted to balancing and benchmarking the network performance, array area, power consumption, as well as manufacturing complexity of the integrated

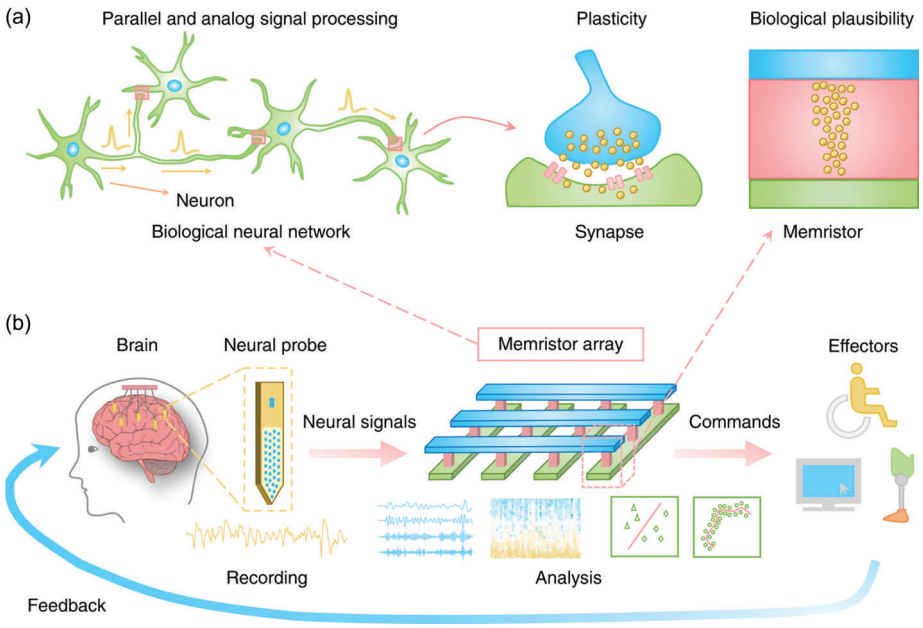

Figure 20. a) Memristor array is analogous to the biological neural network, and the memristor's mechanism is similar to the biological synapse. b) Concept of the brain–machine interface. a,b) Adapted with permission.[160] Copyright 2020, Springer Nature.

system. Such system-level evaluations will require electronic design automation tools. Furthermore, it may be necessary to develop new algorithms or neural networks that can take advantage of the unique properties and integrate structure of memristors and array, especially those that are more similar to the operation principles of the brain.

It should also be noted that studies on artificial neurons are still very limited, especially for their integration. And further investigations are certainly needed to obtain high density artificial neuron elements with biologically plausible functionalities for the construction of bio-inspired computing systems.

Memristor-based neuromorphic hardware has been a rapidly developing area over the last decade, such advancements could potentially complement existing von Neumann computers and find extensive applications in big data and artificial intelligence. However, achieving these goals requires close collaborations between scientists from a wide range of disciplines.

5. Conclusion

We have presented the common electrochemical fundamentals of biological and artificial neurons and synapses. It has been shown that redox-based memristive devices behave in a similar way and demonstrates the same basic properties as their biological counterparts. The ways to design artificial neurons and synapses using the electrochemical-materials approach have been discussed. Device component combinations of different electrode and/or electrolyte materials allow for adjusting and tuning neural and synaptic functionalities.

Using these basic units in more complex circuits has been highlighted in the examples of the variety of two and three-terminal devices and arrays. Different architectures and applications were shown, and the combination and synergy of biological and artificial neurons were showcased. The prospective for further developments and horizon of possible improvements were discussed.

Acknowledgements

The work was funded in part by the project (EMPIR 20FUN06 MEMQuD) that has received funding from the EMPIR program cofinanced by the Participating States and from the European Union's Horizon 2020 research and innovation program.

Open access funding enabled and organized by Projekt DEAL.

Conflict of Interest

The authors declare no conflict of interest.

Keywords

artificial neurons and synapses, brain-inspired computing, memristors, nanoionics

Received: February 28, 2023
Revised: April 22, 2023
Published online:

[1] G. E. Moore, *Proc. IEEE* **1998**, *86*, 82.
[2] R. R. Schaller, *IEEE Spectrum* **1997**, *34*, 52.
[3] M. S. Lundstrom, M. A. Alam, *Science* **2022**, *378*, 722.
[4] M. Horowitz, in *2014 IEEE Int. Solid-State Circuits Conf. Dig. Tech. Pap. (ISSCC)*, IEEE, Piscataway, NJ, USA **2014**, pp. 10–14.
[5] I. L. Markov, *Nature* **2014**, *512*, 147.
[6] H. N. Khan, D. A. Hounshell, E. R. H. Fuchs, *Nat. Electron.* **2018**, *1*, 14.
[7] S. Datta, W. Chakraborty, M. Radosavljevic, *Science* **2022**, *378*, 733.
[8] G. Indiveri, S.-C. Liu, *Proc. IEEE* **2015**, *103*, 1379.
[9] A. S. G. Andrae, T. Edler, *Challenges* **2015**, *6*, 117.
[10] J. Shalf, *Philos. Trans. R. Soc., A* **2020**, *378*, 20190061.
[11] H.-S. P. Wong, S. Salahuddin, *Nat. Nanotechnol.* **2015**, *10*, 191.
[12] A. Sebastian, M. L. Gallo, R. Khaddam-Aljameh, E. Eleftheriou, *Nat. Nanotechnol.* **2020**, *15*, 529.
[13] W. Zhang, B. Gao, J. Tang, P. Yao, S. Yu, M.-F. Chang, H.-J. Yoo, H. Qian, H. Wu, *Nat. Electron.* **2020**, *3*, 371.
[14] M. Huang, M. Schwacke, M. Onen, J. del Alamo, J. Li, B. Yildiz, *Adv. Mater.* **2022**, 2205169.
[15] T. Hasegawa, K. Terabe, T. Tsuruoka, M. Aono, *Adv. Mater.* **2012**, *24*, 252.
[16] P. Robin, T. Emmerich, A. Ismail, A. Niguès, Y. You, G.-H. Nam, A. Keerthi, A. Siria, A. K. Geim, B. Radha, L. Bocquet, *Science* **2023**, *379*, 161.
[17] E. J. Fuller, S. T. Keene, A. Melianas, Z. Wang, S. Agarwal, Y. Li, Y. Tuchman, C. D. James, M. J. Marinella, J. J. Yang, A. Salleo, A. A. Talin, *Science* **2019**, *364*, 570.
[18] K. Terabe, T. Hasegawa, T. Nakayama, M. Aono, *Nature* **2005**, *433*, 47.
[19] J. Chen, B. Luo, Q. Chen, F. Li, Y. Guo, T. Wu, P. Peng, X. Qin, G. Wu, M. Cui, L. Liu, L. Chu, B. Jiang, Y. Li, X. Gong, Y. Chai, Y. Yang, Y. Chen, W. Huang, X. Liu, M. Li, *Adv. Mater.* **2020**, *32*, 1905578.
[20] A. Sood, A. D. Poletayev, D. A. Cogswell, P. M. Csernica, J. T. Mefford, D. Fraggedakis, M. F. Toney, A. M. Lindenberg, M. Z. Bazant, W. C. Chueh, *Nat. Rev. Mater.* **2021**, *6*, 847.
[21] M. Onen, J. Li, B. Yildiz, J. A. Del Alamo, in *2022 Int. Electron Devices Meeting (IEDM)*, IEEE, Piscataway, NJ, USA **2022**, https://doi.org/10.1109/IEDM45625.2022.10019365.
[22] A. J. Tan, M. Huang, C. O. Avci, F. Büttner, M. Mann, W. Hu, C. Mazzoli, S. Wilkins, H. L. Tuller, G. S. D. Beach, *Nat. Mater.* **2019**, *18*, 35.
[23] K. Terabe, T. Tsuchiya, R. Yang, M. Aono, *Nanoscale* **2016**, *8*, 13873.
[24] X. Qiu, K. Narayanapillai, Y. Wu, P. Deorani, D.-H. Yang, W.-S. Noh, J.-H. Park, K.-J. Lee, H.-W. Lee, H. Yang, *Nat. Nanotechnol.* **2015**, *10*, 333.
[25] R. Yang, K. Terabe, G. Liu, T. Tsuruoka, T. Hasegawa, J. K. Gimzewski, M. Aono, *ACS Nano* **2012**, *6*, 9515.
[26] X. Zhu, D. Li, X. Liang, W. D. Lu, *Nat. Mater.* **2019**, *18*, 141.
[27] L. Nagarajan, R. A. De Souza, D. Samuelis, I. Valov, A. Börger, J. Janek, K.-D. Becker, P. C. Schmidt, M. Martin, *Nat. Mater.* **2008**, *7*, 391.
[28] W. Chen, N. Chamele, Y. Gonzalez-Velo, H. J. Barnaby, M. N. Kozicki, *IEEE Electron Device Lett.* **2017**, *38*, 1244.
[29] A. Melianas, T. J. Quill, G. LeCroy, Y. Tuchman, H. v. Loo, S. T. Keene, A. Giovannitti, H. R. Lee, I. P. Maria, I. McCulloch, A. Salleo, *Sci. Adv.* **2020**, *6*, eabb2958.
[30] J. L. Taggart, W. Chen, Y. Gonzalez-Velo, H. J. Barnaby, K. Holbert, M. N. Kozicki, *IEEE Trans. Nucl. Sci.* **2018**, *65*, 192.
[31] I. Valov, W. D. Lu, *Nanoscale* **2016**, *8*, 13828.
[32] M.-J. Lee, C. B. Lee, D. Lee, S. R. Lee, M. Chang, J. H. Hur, Y.-B. Kim, C.-J. Kim, D. H. Seo, S. Seo, U.-I. Chung, I.-K. Yoo, K. Kim, *Nat. Mater.* **2011**, *10*, 625.

[33] M. Son, J. Lee, J. Park, J. Shin, G. Choi, S. Jung, W. Lee, S. Kim, S. Park, H. Hwang, *IEEE Electron Device Lett.* **2011**, *32*, 1579.
[34] Q. Luo, J. Yu, X. Zhang, K.-H. Xue, J.-H. Yuan, Y. Cheng, T. Gong, H. Lv, X. Xu, P. Yuan, J. Yin, L. Tai, S. Long, Q. Liu, X. Miao, J. Li, M. Liu, in *2019 Symp. on VLSI Technology*, IEEE, Piscataway, NJ, USA **2019**, pp. T236–T237.
[35] *Nanoelectronics and Information Technology: Advanced Electronic Materials and Novel Devices* (Ed: R. Waser), Wiley-VCH, Weinheim, Germany **2012**.
[36] A. Chen, *Solid-State Electron.* **2016**, *125*, 25.
[37] *Mem-Elements for Neuromorphic Circuits with Artificial Intelligence Applications* (Eds: C. Volos, V.-T. Pham), Academic Press, Amsterdam, The Netherlands **2021**.
[38] M. Prezioso, F. Merrikh-Bayat, B. D. Hoskins, G. C. Adam, K. K. Likharev, D. B. Strukov, *Nature* **2015**, *521*, 61.
[39] Q. Huo, Y. Yang, Y. Wang, D. Lei, X. Fu, Q. Ren, X. Xu, Q. Luo, G. Xing, C. Chen, X. Si, H. Wu, Y. Yuan, Q. Li, X. Li, X. Wang, M.-F. Chang, F. Zhang, M. Liu, *Nat. Electron.* **2022**, *5*, 469.
[40] J. Huang, A. Serb, S. Stathopoulos, T. Prodromakis, *Neuromorph. Comput. Eng.* **2023**, *3*, 014003.
[41] J. Borghetti, G. S. Snider, P. J. Kuekes, J. J. Yang, D. R. Stewart, R. S. Williams, *Nature* **2010**, *464*, 873.
[42] W. Wan, R. Kubendran, C. Schaefer, S. B. Eryilmaz, W. Zhang, D. Wu, S. Deiss, P. Raina, H. Qian, B. Gao, S. Joshi, H. Wu, H.-S. P. Wong, G. Cauwenberghs, *Nature* **2022**, *608*, 504.
[43] F. Cai, J. M. Correll, S. H. Lee, Y. Lim, V. Bothra, Z. Zhang, M. P. Flynn, W. D. Lu, *Nat. Electron.* **2019**, *2*, 290.
[44] S. D. Spetalnick, M. Chang, B. Crafton, W.-S. Khwa, Y.-D. Chih, M.-F. Chang, A. Raychowdhury, in *2022 IEEE Int. Solid-State Circuits Conf. (ISSCC)*, IEEE, Piscataway, NJ, USA **2022**, https://doi.org/10.1109/ISSCC42614.2022.9731725.
[45] P. Yao, H. Wu, B. Gao, J. Tang, Q. Zhang, W. Zhang, J. J. Yang, H. Qian, *Nature* **2020**, *577*, 641.
[46] J. Cong, B. Xiao, *IEEE Trans. VLSI Syst.* **2014**, *22*, 864.
[47] Y. Y. Liauw, Z. Zhang, W. Kim, A. E. Gamal, S. S. Wong, in *2012 IEEE Int. Solid-State Circuits Conf.*, IEEE, Piscataway, NJ, USA **2012**, pp. 406–408.
[48] R. Nebashi, N. Banno, M. Miyamura, X. Bai, K. Funahashi, K. Okamoto, N. Iguchi, H. Numata, T. Sugibayashi, T. Sakamoto, M. Tada, in *2020 30th Int. Conf. on Field-Programmable Logic and Applications (FPL)*, IEEE, Piscataway, NJ, USA **2020**, pp. 323–327.
[49] T.-H. Hsu, Y.-C. Chiu, W.-C. Wei, Y.-C. Lo, C.-C. Lo, R.-S. Liu, K.-T. Tang, M.-F. Chang, C.-C. Hsieh, in *2019 IEEE Int. Electron Devices Meeting (IEDM)*, IEEE, Piscataway, NJ, USA **2019**, https://doi.org/10.1109/IEDM19573.2019.8993452.
[50] Y. Wang, Y. Gong, L. Yang, Z. Xiong, Z. Lv, X. Xing, Y. Zhou, B. Zhang, C. Su, Q. Liao, S.-T. Han, *Adv. Funct. Mater.* **2021**, *31*, 2100144.
[51] T. Wan, B. Shao, S. Ma, Y. Zhou, Q. Li, Y. Chai, *Adv. Mater.* **2022**, https://doi.org/10.1002/adma.202203830.
[52] D. Ielmini, H.-S. P. Wong, *Nat. Electron.* **2018**, *1*, 333.
[53] J.-M. Hung, Y.-H. Huang, S.-P. Huang, F.-C. Chang, T.-H. Wen, C.-I. Su, W.-S. Khwa, C.-C. Lo, R.-S. Liu, C.-C. Hsieh, K.-T. Tang, Y.-D. Chih, T.-Y. J. Chang, M.-F. Chang, in *2022 IEEE Int. Solid-State Circuits Conf. (ISSCC)*, IEEE, Piscataway, NJ, USA **2022**, https://doi.org/10.1109/ISSCC42614.2022.9731715.
[54] M. A. Zidan, J. P. Strachan, W. D. Lu, *Nat. Electron.* **2018**, *1*, 22.
[55] S. Kumar, X. Wang, J. P. Strachan, Y. Yang, W. D. Lu, *Nat. Rev. Mater.* **2022**, *7*, 575.
[56] V. K. Sangwan, M. C. Hersam, *Nat. Nanotechnol.* **2020**, *15*, 517.
[57] T. Serrano-Gotarredona, T. Masquelier, T. Prodromakis, G. Indiveri, B. Linares-Barranco, *Front. Neurosci.* **2013**, *7*, 2.
[58] Z. Wang, S. Joshi, S. E. Savel'ev, H. Jiang, R. Midya, P. Lin, M. Hu, N. Ge, J. P. Strachan, Z. Li, Q. Wu, M. Barnell, G.-L. Li, H. L. Xin, R. S. Williams, Q. Xia, J. J. Yang, *Nat. Mater.* **2017**, *16*, 101.
[59] L. Zhou, J.-Y. Mao, Y. Ren, J.-Q. Yang, S.-R. Zhang, Y. Zhou, Q. Liao, Y.-J. Zeng, H. Shan, Z. Xu, J. Fu, Y. Wang, X. Chen, Z. Lv, S.-T. Han, V. A. L. Roy, *Small* **2018**, *14*, 1800288.
[60] Z. Wang, T. Zeng, Y. Ren, Y. Lin, H. Xu, X. Zhao, Y. Liu, D. Ielmini, *Nat. Commun.* **2020**, *11*, 1510.
[61] I. Valov, M. N. Kozicki, *J. Phys. Appl. Phys.* **2013**, *46*, 074005.
[62] Y. Yang, P. Gao, L. Li, X. Pan, S. Tappertzhofen, S. Choi, R. Waser, I. Valov, W. D. Lu, *Nat. Commun.* **2014**, *5*, 4232.
[63] S. H. Jo, T. Chang, I. Ebong, B. B. Bhadviya, P. Mazumder, W. Lu, *Nano Lett.* **2010**, *10*, 1297.
[64] N. Qiao, H. Mostafa, F. Corradi, M. Osswald, F. Stefanini, D. Sumislawska, G. Indiveri, *Front. Neurosci.* **2015**, *9*, 141.
[65] Y. Yang, P. Gao, S. Gaba, T. Chang, X. Pan, W. Lu, *Nat. Commun.* **2012**, *3*, 732.
[66] Y. Yang, M. Yin, Z. Yu, Z. Wang, T. Zhang, Y. Cai, W. D. Lu, R. Huang, *Adv. Electron. Mater.* **2017**, *3*, 1700032.
[67] S. Kim, C. Du, P. Sheridan, W. Ma, S. Choi, W. D. Lu, *Nano Lett.* **2015**, *15*, 2203.
[68] K.-H. Kim, S. Gaba, D. Wheeler, J. M. Cruz-Albrecht, T. Hussain, N. Srinivasa, W. Lu, *Nano Lett.* **2012**, *12*, 389.
[69] H. Hihara, A. Iwasaki, N. Tamagawa, M. Kuribayashi, M. Hashimoto, Y. Mitsuyama, H. Ochi, H. Onodera, H. Kanbara, K. Wakabayashi, M. Tada, *Proc. SPIE* **2016**, *9973*, 99730S-1.
[70] X. Bai, N. Banno, M. Miyamura, R. Nebashi, K. Okamoto, H. Numata, N. Iguchi, M. Hashimoto, T. Sugibayashi, T. Sakamoto, M. Tada, *IEEE J. Solid-State Circuits* **2022**, *57*, 2250.
[71] T. Tsuchiya, T. Nakayama, K. Ariga, *Appl. Phys. Express* **2022**, *15*, 100101.
[72] D. Ielmini, *Semicond. Sci. Technol.* **2016**, *31*, 063002.
[73] J. J. Yang, D. B. Strukov, D. R. Stewart, *Nat. Nanotechnol.* **2013**, *8*, 13.
[74] D. S. Jeong, C. S. Hwang, *Adv. Mater.* **2018**, *30*, 1704729.
[75] Y. Li, Z. Wang, R. Midya, Q. Xia, J. J. Yang, *J. Phys. Appl. Phys.* **2018**, *51*, 503002.
[76] Z. Wang, H. Wu, G. W. Burr, C. S. Hwang, K. L. Wang, Q. Xia, J. J. Yang, *Nat. Rev. Mater.* **2020**, *5*, 173.
[77] S. Choi, J. Yang, G. Wang, *Adv. Mater.* **2020**, *32*, 2004659.
[78] J. Tang, F. Yuan, X. Shen, Z. Wang, M. Rao, Y. He, Y. Sun, X. Li, W. Zhang, Y. Li, B. Gao, H. Qian, G. Bi, S. Song, J. J. Yang, H. Wu, *Adv. Mater.* **2019**, *31*, 1902761.
[79] J.-K. Han, S.-Y. Yun, S.-W. Lee, J.-M. Yu, Y.-K. Choi, *Adv. Funct. Mater.* **2022**, *32*, 2204102.
[80] S. Wang, R. Wang, Y. Cao, X. Ma, H. Wang, Y. Hao, *Adv. Electron. Mater.* **2023**, *9*, 2200972.
[81] H. Bian, Y. Y. Goh, Y. Liu, H. Ling, L. Xie, X. Liu, *Adv. Mater.* **2021**, *33*, 2006469.
[82] A. Mehonic, A. Sebastian, B. Rajendran, O. Simeone, E. Vasilaki, A. J. Kenyon, *Adv. Intell. Syst.* **2020**, *2*, 2000085.
[83] A. L. Hodgkin, A. F. Huxley, *J. Physiol.* **1952**, *117*, 500.
[84] E. Karatan, Z. Han, B. Kay, in *Encyclopedia of Molecular Cell Biology and Molecular Medicine*, (Ed: R. A. Meyers), Wiley-VCH, Weinheim, Germany **2006**, Supplement 11.
[85] O. S. Andersen, H. I. Ingólfsson, J. A. Lundbæk, in *Wiley Encyclopedia of Chemical Biology*, (Ed: T. P. Begley), John Wiley & Sons, Inc., Hoboken, NJ, USA **2008**, pp. 1.
[86] M. Chappell, S. Payne, *Physiology for Engineers*, Springer, Cham, Switzerland **2016**.
[87] R. Sacco, G. Guidoboni, A. G. Mauri, in *A Comprehensive Physically Based Approach to Modeling in Bioengineering and Life Sciences*, (Eds: R. Sacco, G. Guidoboni, A. G. Mauri), Elsevier, Amsterdam, The Netherlands **2019**, pp. 425.
[88] G. B. Ermentrout, D. H. Terman, *Mathematical Foundations of Neuroscience*, Springer, New York **2010**.

[89] B. Hille, *Ionic Channels of Excitable Membranes*, Sinauer, Sunderland, MA, USA **2001**.
[90] A. L. Hodgkin, A. F. Huxley, B. Katz, *J. Physiol.* **1952**, *116*, 424.
[91] G. B. Ermentrout, D. H. Terman, in *Mathematical Foundations of Neuroscience* (Eds: G. B. Ermentrout, D. H. Terman), Springer, New York **2010**, pp. 1.
[92] T. Nowotny, R. Levi, in *Encyclopedia of Computational Neuroscience* (Eds: D. Jaeger, R. Jung), Springer, New York **2014**, pp. 1–5.
[93] T. C. Südhof, R. C. Malenka, *Neuron* **2008**, *60*, 469.
[94] J. L. Salzer, *Cold Spring Harbor Perspect. Biol.* **2015**, *7*, a020529.
[95] E. M. Boutzoukas, A. J. Woods, in *Encyclopedia of Gerontology and Population Aging* (Eds: D. Gu, M. E. Dupre), Springer International Publishing, Cham, Switzerland **2021**, pp. 3459.
[96] W. Senn, J.-P. Pfister, in *Encyclopedia of Computational Neuroscience* (Eds.: D. Jaeger, R. Jung), Springer, New York **2014**, pp. 1–10.
[97] B. Linares-Barranco, T. Serrano-Gotarredona, L. Camuñas-Mesa, J. Perez-Carrasco, C. Zamarreño-Ramos, T. Masquelier, *Front. Neurosci.* **2011**, *5*, 26.
[98] G. Bi, M. Poo, *J. Neurosci.* **1998**, *18*, 10464.
[99] S. G. Hormuzdi, M. A. Filippov, G. Mitropoulou, H. Monyer, R. Bruzzone, *Biochim. Biophys. Acta* **2004**, *1662*, 113.
[100] A. E. Pereda, S. Curti, G. Hoge, R. Cachope, C. E. Flores, J. E. Rash, *Biochim. Biophys. Acta* **2013**, *1828*, 134.
[101] E. A. Eugenin, D. Basilio, J. C. Sáez, J. A. Orellana, C. S. Raine, F. Bukauskas, M. V. L. Bennett, J. W. Berman, *J. Neuroimmune Pharmacol.* **2012**, *7*, 499.
[102] V. S. Ramachandran, *Encyclopedia of the Human Brain*, Academic Press, San Diego, CA, USA **2002**.
[103] J. S. Haas, B. Zavala, C. E. Landisman, *Science* **2011**, *334*, 389.
[104] Q. Xia, J. J. Yang, *Nat. Mater.* **2019**, *18*, 309.
[105] I. Valov, E. Linn, S. Tappertzhofen, S. Schmelzer, J. van den Hurk, F. Lentz, R. Waser, *Nat. Commun.* **2013**, *4*, 1771.
[106] H. Yeon, P. Lin, C. Choi, S. H. Tan, Y. Park, D. Lee, J. Lee, F. Xu, B. Gao, H. Wu, H. Qian, Y. Nie, S. Kim, J. Kim, *Nat. Nanotechnol.* **2020**, *15*, 574.
[107] M. Congiu, L. G. S. Albano, O. Nunes-Neto, C. f. O. Graeff, *Electron. Lett.* **2016**, *52*, 1871.
[108] A. Mehonic, A. J. Kenyon, *Front. Neurosci.* **2016**, *10*, 57.
[109] J.-W. Jang, B. Attarimashalkoubeh, A. Prakash, H. Hwang, Y.-H. Jeong, *IEEE Trans. Electron Devices* **2016**, *63*, 2610.
[110] G. Palma, M. Suri, D. Querlioz, E. Vianello, B. De Salvo, in *2013 IEEE/ACM Int. Symp. on Nanoscale Architectures (NANOARCH)*, IEEE, Piscataway, NJ, USA **2013**, pp. 95–100.
[111] T. C. Jackson, A. A. Sharma, J. A. Bain, J. A. Weldon, L. Pileggi, *IEEE J. Emerging Sel. Top. Circuits Syst.* **2015**, *5*, 230.
[112] X. Zhang, W. Wang, Q. Liu, X. Zhao, J. Wei, R. Cao, Z. Yao, X. Zhu, F. Zhang, H. Lv, S. Long, M. Liu, *IEEE Electron Device Lett.* **2018**, *39*, 308.
[113] T. Tuma, A. Pantazi, M. L. Gallo, A. Sebastian, E. Eleftheriou, *Nat. Nanotechnol.* **2016**, *11*, 693.
[114] I. Chakraborty, G. Saha, A. Sengupta, K. Roy, *Sci. Rep.* **2018**, *8*, 12980.
[115] G. Pedretti, P. Mannocci, S. Hashemkhani, V. Milo, O. Melnic, E. Chicca, D. Ielmini, *IEEE J. Explor. Solid-State Comput. Devices Circuits* **2020**, *6*, 89.
[116] A. Pantazi, S. Woźniak, T. Tuma, E. Eleftheriou, *Nanotechnology* **2016**, *27*, 355205.
[117] M.-H. Wu, M.-C. Hong, C.-C. Chang, P. Sahu, J.-H. Wei, H.-Y. Lee, S.-S. Shcu, T.-H. Hou, in *2019 Symp. VLSI on Technology*, IEEE, Piscataway, NJ, USA **2019**, pp. T34–T35.
[118] J. Cai, B. Fang, L. Zhang, W. Lv, B. Zhang, T. Zhou, G. Finocchio, Z. Zeng, *Phys. Rev. Appl.* **2019**, *11*, 034015.
[119] D. Zhang, L. Zeng, K. Cao, M. Wang, S. Peng, Y. Zhang, Y. Zhang, J.-O. Klein, Y. Wang, W. Zhao, *IEEE Trans. Biomed. Circuits Syst.* **2016**, *10*, 828.
[120] D. Lee, M. Kwak, K. Moon, W. Choi, J. Park, J. Yoo, J. Song, S. Lim, C. Sung, W. Banerjee, H. Hwang, *Adv. Electron. Mater.* **2019**, *5*, 1800866.
[121] W. Yi, K. K. Tsang, S. K. Lam, X. Bai, J. A. Crowell, E. A. Flores, *Nat. Commun.* **2018**, *9*, 4661.
[122] P. Stoliar, J. Tranchant, B. Corraze, E. Janod, M.-P. Besland, F. Tesler, M. Rozenberg, L. Cario, *Adv. Funct. Mater.* **2017**, *27*, 1604740.
[123] S. Kumar, R. S. Williams, Z. Wang, *Nature* **2020**, *585*, 518.
[124] M. Jerry, A. Parihar, B. Grisafe, A. Raychowdhury, S. Datta, in *2017 Symp. on VLSI Technology*, IEEE, Piscataway, NJ, USA **2017**, pp. T186–T187.
[125] W. A. Catterall, A. P. Few, *Neuron* **2008**, *59*, 882.
[126] R. D. Burgoyne, *Nat. Rev. Neurosci.* **2007**, *8*, 182.
[127] K. S. Woo, J. Kim, J. Han, J. M. Choi, W. Kim, C. S. Hwang, *Adv. Intell. Syst.* **2021**, *3*, 2100062.
[128] Z. Wang, M. Rao, J.-W. Han, J. Zhang, P. Lin, Y. Li, C. Li, W. Song, S. Asapu, R. Midya, Y. Zhuo, H. Jiang, J. H. Yoon, N. K. Upadhyay, S. Joshi, M. Hu, J. P. Strachan, M. Barnell, Q. Wu, H. Wu, Q. Qiu, R. S. Williams, Q. Xia, J. J. Yang, *Nat. Commun.* **2018**, *9*, 3208.
[129] Z. Wang, S. Joshi, S. Savel'ev, W. Song, R. Midya, Y. Li, M. Rao, P. Yan, S. Asapu, Y. Zhuo, H. Jiang, P. Lin, C. Li, J. H. Yoon, N. K. Upadhyay, J. Zhang, M. Hu, J. P. Strachan, M. Barnell, Q. Wu, H. Wu, R. S. Williams, Q. Xia, J. J. Yang, *Nat. Electron.* **2018**, *1*, 137.
[130] G. Indiveri, in *Proc. of the 2003 Int. Symp. on Circuits and Systems (ISCAS)*, IEEE, Piscataway, NJ, USA **2003**, pp. IV820–IV823.
[131] T. Garnier Artiñano, V. Andalibi, I. Atula, M. Maestri, S. Vanni, *Front. Comput. Neurosci.* **2023**, *17*, 1011814.
[132] N. Fourcaud-Trocmé, D. Hansel, C. van Vreeswijk, N. Brunel, *J. Neurosci.* **2003**, *23*, 11628.
[133] T. Górski, D. Depannemaecker, A. Destexhe, *Neural Comput.* **2021**, *33*, 41.
[134] R. Brette, W. Gerstner, *J. Neurophysiol.* **2005**, *94*, 3637.
[135] L. Badel, S. Lefort, R. Brette, C. C. H. Petersen, W. Gerstner, M. J. E. Richardson, *J. Neurophysiol.* **2008**, *99*, 656.
[136] P. E. Latham, B. J. Richmond, P. G. Nelson, S. Nirenberg, *J. Neurophysiol.* **2000**, *83*, 808.
[137] M. J. E. Richardson, *Phys. Rev. E* **2009**, *80*, 021928.
[138] G. Milano, M. Luebben, Z. Ma, R. Dunin-Borkowski, L. Boarino, C. F. Pirri, R. Waser, C. Ricciardi, I. Valov, *Nat. Commun.* **2018**, *9*, 5151.
[139] M. Prezioso, M. R. Mahmoodi, F. M. Bayat, H. Nili, H. Kim, A. Vincent, D. B. Strukov, *Nat. Commun.* **2018**, *9*, 5311.
[140] M. Lübben, F. Cüppers, J. Mohr, M. von Witzleben, U. Breuer, R. Waser, C. Neumann, I. Valov, *Sci. Adv.* **2020**, *6*, eaaz9079.
[141] M. Lübben, S. Wiefels, R. Waser, I. Valov, *Adv. Electron. Mater.* **2018**, *4*, 1700458.
[142] S. Tappertzhofen, R. Waser, I. Valov, *ChemElectroChem* **2014**, *1*, 1287.
[143] A. Mehonic, T. Gerard, A. J. Kenyon, *Appl. Phys. Lett.* **2017**, *111*, 233502.
[144] A. Belmonte, R. Degraeve, A. Fantini, W. Kim, M. Houssa, M. Jurczak, L. Goux, *Appl. Phys. Lett.* **2014**, *104*, 233508.
[145] S. Dutta, V. Kumar, A. Shukla, N. R. Mohapatra, U. Ganguly, *Sci. Rep.* **2017**, *7*, 8257.
[146] L. Gao, P.-Y. Chen, S. Yu, *Appl. Phys. Lett.* **2017**, *111*, 103503.
[147] M. D. Pickett, G. Medeiros-Ribeiro, R. S. Williams, *Nat. Mater.* **2013**, *12*, 114.
[148] J. Lin, Annadi, S. S., C. Chen, L. Stan, K. V. L. V. Achari, S. Ramanathan, S. Guha, in *2016 IEEE Int. Electron Devices Meeting (IEDM)*, IEEE, Piscataway, NJ, USA **2016**, https://doi.org/10.1109/IEDM.2016.7838541.
[149] Q. Duan, Z. Jing, X. Zou, Y. Wang, K. Yang, T. Zhang, S. Wu, R. Huang, Y. Yang, *Nat. Commun.* **2020**, *11*, 3399.
[150] J. A. Cardin, M. Carlén, K. Meletis, U. Knoblich, F. Zhang, K. Deisseroth, L.-H. Tsai, C. I. Moore, *Nature* **2009**, *459*, 663.

[151] A. Schnitzler, J. Gross, *Nat. Rev. Neurosci.* **2005**, *6*, 285.
[152] Y. Zhang, W. He, Y. Wu, K. Huang, Y. Shen, J. Su, Y. Wang, Z. Zhang, X. Ji, G. Li, H. Zhang, S. Song, H. Li, L. Sun, R. Zhao, L. Shi, *Small* **2018**, *14*, 1802188.
[153] Y. Li, J. Tang, B. Gao, X. Li, Y. Xi, W. Zhang, H. Qian, H. Wu, *J. Semicond.* **2021**, *42*, 064101.
[154] S. Yu, Y. Wu, R. Jeyasingh, D. Kuzum, H.-S. P. Wong, *IEEE Trans. Electron Devices* **2011**, *58*, 2729.
[155] Z. Wang, M. Yin, T. Zhang, Y. Cai, Y. Wang, Y. Yang, R. Huang, *Nanoscale* **2016**, *8*, 14015.
[156] Q. Wu, H. Wang, Q. Luo, W. Banerjee, J. Cao, X. Zhang, F. Wu, Q. Liu, L. Li, M. Liu, *Nanoscale* **2018**, *10*, 5875.
[157] M. Hennig, *Front. Comput. Neurosci.* **2013**, *7*, 45.
[158] W. C. Abraham, M. F. Bear, *Trends Neurosci.* **1996**, *19*, 126.
[159] M. Chistiakova, N. M. Bannon, M. Bazhenov, M. Volgushev, *Neuroscientist* **2014**, *20*, 483.
[160] Z. Liu, J. Tang, B. Gao, P. Yao, X. Li, D. Liu, Y. Zhou, H. Qian, B. Hong, H. Wu, *Nat. Commun.* **2020**, *11*, 4234.
[161] X. Zhu, Q. Wang, W. D. Lu, *Nat. Commun.* **2020**, *11*, 2439.
[162] Q. Wang, X. Wang, S. H. Lee, F.-H. Meng, W. D. Lu, in *2019 IEEE Int. Electron Devices Meeting (IEDM)*, IEEE, Piscataway, NJ, USA **2019**, https://doi.org/10.1109/IEDM19573.2019.8993641.
[163] M. Hu, C. E. Graves, C. Li, Y. Li, N. Ge, E. Montgomery, N. Davila, H. Jiang, R. S. Williams, J. J. Yang, Q. Xia, J. P. Strachan, *Adv. Mater.* **2018**, *30*, 1705914.
[164] J. H. Shin, Y. J. Jeong, M. A. Zidan, Q. Wang, W. D. Lu, in *2018 IEEE Int. Electron Devices Meeting (IEDM)*, IEEE, Piscataway, NJ, USA **2018**, https://doi.org/10.1109/IEDM.2018.8614698.
[165] H. Kim, M. R. Mahmoodi, H. Nili, D. B. Strukov, *Nat. Commun.* **2021**, *12*, 5198.
[166] S. Pi, C. Li, H. Jiang, W. Xia, H. Xin, J. J. Yang, Q. Xia, *Nat. Nanotechnol.* **2019**, *14*, 35.
[167] G. C. Adam, B. D. Hoskins, M. Prezioso, F. Merrikh-Bayat, B. Chakrabarti, D. B. Strukov, *IEEE Trans. Electron Devices* **2017**, *64*, 312.
[168] C. Li, L. Han, H. Jiang, M.-H. Jang, P. Lin, Q. Wu, M. Barnell, J. J. Yang, H. L. Xin, Q. Xia, *Nat. Commun.* **2017**, *8*, 15666.
[169] T.-Y. Wang, J.-L. Meng, L. Chen, H. Zhu, Q.-Q. Sun, S.-J. Ding, W.-Z. Bao, D. W. Zhang, *InfoMat* **2021**, *3*, 212.
[170] S. Yu, H.-Y. Chen, B. Gao, J. Kang, H.-S. P. Wong, *ACS Nano* **2013**, *7*, 2320.
[171] L. Zhang, S. Cosemans, D. J. Wouters, B. Govoreanu, G. Groeseneken, M. Jurczak, in *2013 5th IEEE Int. Memory Workshop*, IEEE, Piscataway, NJ, USA **2013**, pp. 155–158.
[172] P.-Y. Chen, Z. Li, S. Yu, *IEEE Trans. VLSI Syst.* **2016**, *24*, 3460.
[173] A. Jain, R. E. Jones, R. Chatterjee, S. Pozder, *IEEE Trans. Compon. Packag. Technol.* **2010**, *33*, 56.
[174] J. L. Ayala, A. Sridhar, D. Cuesta, *Integration* **2010**, *43*, 327.
[175] J. P. Strachan, D. B. Strukov, J. Borghetti, J. J. Yang, G. Medeiros-Ribeiro, R. S. Williams, *Nanotechnology* **2011**, *22*, 254015.
[176] P. Sun, N. Lu, L. Li, Y. Li, H. Wang, H. Lv, Q. Liu, S. Long, S. Liu, M. Liu, *Sci. Rep.* **2015**, *5*, 13504.
[177] D. B. Strukov, R. S. Williams, *Proc. Natl. Acad. Sci. USA* **2009**, *106*, 20155.
[178] C. Li, M. Hu, Y. Li, H. Jiang, N. Ge, E. Montgomery, J. Zhang, W. Song, N. Dávila, C. E. Graves, Z. Li, J. P. Strachan, P. Lin, Z. Wang, M. Barnell, Q. Wu, R. S. Williams, J. J. Yang, Q. Xia, *Nat. Electron.* **2018**, *1*, 52.
[179] P. Lin, C. Li, Z. Wang, Y. Li, H. Jiang, W. Song, M. Rao, Y. Zhuo, N. K. Upadhyay, M. Barnell, Q. Wu, J. J. Yang, Q. Xia, *Nat. Electron.* **2020**, *3*, 225.
[180] H. Valavi, P. J. Ramadge, E. Nestler, N. Verma, *IEEE J. Solid-State Circuits* **2019**, *54*, 1789.
[181] S. Hatayama, Y. Sutou, S. Shindo, Y. Saito, Y.-H. Song, D. Ando, J. Koike, *ACS Appl. Mater. Interfaces* **2018**, *10*, 2725.
[182] T. Mikolajick, S. Slesazeck, M. H. Park, U. Schroeder, *MRS Bull.* **2018**, *43*, 340.
[183] J. Tang, D. Bishop, S. Kim, M. Copel, T. Gokmen, T. Todorov, S. Shin, K.-T. Lee, P. Solomon, K. Chan, W. Haensch, J. Rozen, in *2018 IEEE Int. Electron Devices Meeting (IEDM)*, IEEE, Piscataway, NJ, USA **2018**, https://doi.org/10.1109/IEDM.2018.8614551.
[184] P. Gkoupidenis, D. A. Koutsouras, G. G. Malliaras, *Nat. Commun.* **2017**, *8*, 15448.
[185] Y. van de Burgt, E. Lubberman, E. J. Fuller, S. T. Keene, G. C. Faria, S. Agarwal, M. J. Marinella, A. Alec Talin, A. Salleo, *Nat. Mater.* **2017**, *16*, 414.
[186] J. Zhu, Y. Yang, R. Jia, Z. Liang, W. Zhu, Z. U. Rehman, L. Bao, X. Zhang, Y. Cai, L. Song, R. Huang, *Adv. Mater.* **2018**, *30*, 1800195.
[187] S. Seo, S.-H. Jo, S. Kim, J. Shim, S. Oh, J.-H. Kim, K. Heo, J.-W. Choi, C. Choi, S. Oh, D. Kuzum, H.-S. P. Wong, J.-H. Park, *Nat. Commun.* **2018**, *9*, 5106.
[188] V. K. Sangwan, H.-S. Lee, H. Bergeron, I. Balla, M. E. Beck, K.-S. Chen, M. C. Hersam, *Nature* **2018**, *554*, 500.
[189] Y. Choi, S. Oh, C. Qian, J.-H. Park, J. H. Cho, *Nat. Commun.* **2020**, *11*, 4595.
[190] J. Lee, R. D. Nikam, D. Kim, H. Hwang, in *2022 Int. Electron Devices Meeting (IEDM)*, IEEE, Piscataway, NJ, USA **2022**, https://doi.org/10.1109/IEDM45625.2022.10019326.
[191] C. Lee, W. Choi, M. Kwak, S. Kim, H. Hwang, in *2021 Symp. VLSI Technol.*, IEEE, Piscataway, NJ, USA **2021**, pp. 1–2, https://ieeexplore.ieee.org/abstract/document/9508687.
[192] F. M. Bayat, M. Prezioso, B. Chakrabarti, H. Nili, I. Kataeva, D. Strukov, *Nat. Commun.* **2018**, *9*, 2331.
[193] C. Li, D. Belkin, Y. Li, P. Yan, M. Hu, N. Ge, H. Jiang, E. Montgomery, P. Lin, Z. Wang, W. Song, J. P. Strachan, M. Barnell, Q. Wu, R. S. Williams, J. J. Yang, Q. Xia, *Nat. Commun.* **2018**, *9*, 2385.
[194] O. Tunali, M. C. Morgul, M. Altun, *IEEE Micro* **2018**, *38*, 22.
[195] Y. Zheng, H. Ravichandran, T. F. Schranghamer, N. Trainor, J. M. Redwing, S. Das, *Nat. Commun.* **2022**, *13*, 5578.
[196] A. Serb, A. Corna, R. George, A. Khiat, F. Rocchi, M. Reato, M. Maschietto, C. Mayr, G. Indiveri, S. Vassanelli, T. Prodromakis, *Sci. Rep.* **2020**, *10*, 2590.
[197] C. Li, C. Lammie, X. Dong, A. Amirsoleimani, M. R. Azghadi, R. Genov, *IEEE Trans. Biomed. Circuits Syst.* **2022**, *16*, 609.

Shaochuan Chen is currently a Ph.D. student in the Faculty of Electrical Engineering and Information Technology at RWTH Aachen University, Germany. He received his Bachelor's degree in engineering from North China Electric Power University in 2016. His research interests include oxides and 2D materials based memristive systems, with a focus on the investigation of underlying physical and electrochemical processes, switching dynamics, the design and tunning of memristive functionalities, and their applications for memory, neuromorphic and computation-in-memory applications.

Teng Zhang is a postdoctoral researcher at the School of Integrated Circuits, Peking University. Before taking this position, he received his Ph.D. degree in 2021 under the supervision of Prof. Ru Huang at the Institute of Microelectronics, School of Electronics Engineering and Computer Science, Peking University. Currently, he works with Prof. Yuchao Yang on optimization and integration of nanoscale devices, and his interests lie in the emerging memristive devices and their applications in sensing, logic and neuromorphic computing.

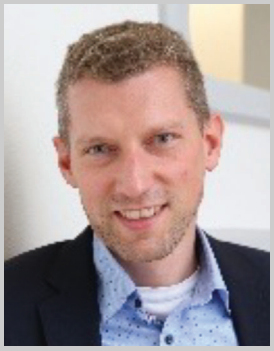

Stefan Tappertzhofen (*1984) studied electrical engineering and information technology and received his Ph.D. in 2014 at RWTH Aachen University, Germany. From 2014 to 2016 he worked as postdoctoral research associate at the Department of Engineering (Electronic Engineering Division), University of Cambridge, United Kingdom. Afterward, he worked as a research and development manager for thin-film metrology at aixACCT Systems, Aachen, Germany. Since 2020 he is professor in micro- and nanoelectronics at TU Dortmund University, Germany. His research is focused on novel multifunctional materials, memristive systems and circuits, and quantum- and nanotechnology.

Yuchao Yang is a Boya distinguished professor at School of Integrated Circuits, Peking University. He serves asdeputy dean for School of Electronic and Computer Engineering, and director of Center for Brain Inspired Chips. His research interests include memristors, neuromorphic computing, and in-memory computing. He has published over 140 papers in high-profile journals and conferences such as *Nature Electronics*, *Nature Reviews Materials*, *Nature Communications*, *Nature Nanotechnology*, *Science Advances*, *Advanced Materials*, *Nano Letters*, *IEDM*, etc. He was invited to give >40 keynote/invited talks on international conferences and serves as TPC chair or member for 9 international conferences.

Ilia Valov is a professor in electrochemistry at the Institute of Electrochemistry and Energy Systems, Bulgarian Academy of Sciences, Bulgaria and leads a group Nanoelectrochemistry at Forschugszentrum Jülich, Germany. His research interests and activities are concentrated on electrochemical and, in general, physicochemical phenomena at the nano and sub-nanoscale, such as mass and charge transport, electric double layer, point defects, surfaces and interfaces with a focus on resistive switching memories, memristive and neuromorphic devices, energy conversion and electrocatalysis (water splitting). Special attention is paid to the relation between materials chemistry, structure and properties, materials design and functionalities.